AGU PUBLICATIONS

JGR

Journal of Geophysical Research: Oceans

RESEARCH ARTICLE

10.1002/2015JC011452

Special Section:
Physical Processes Responsible for Material Transport in the Gulf of Mexico for Oil Spill Applications

Observations of bubbles in natural seep flares at MC 118 and GC 600 using in situ quantitative imaging

Binbin Wang[1], Scott A. Socolofsky[1], John A. Breier[2,3], and Jeffrey S. Seewald[4]

[1]Zachry Department of Civil Engineering, Texas A&M University, College Station, Texas, USA, [2]Coastal Studies Program, University of Texas, Rio Grande Valley, Brownsville, Texas, USA, [3]Applied Ocean Physics and Engineering, Woods Hole Oceanographic Institution, Woods Hole, Massachusetts, USA, [4]Marine Chemistry and Geochemistry, Woods Hole Oceanographic Institution, Woods Hole, Massachusetts, USA

Key Points:
- Seep bubbles survive to the boundary of the hydrate stability zone
- Rise speed of bubbles are correlated with the trajectories
- Size evolution of the hydrate bubbles agrees with predicted mass transfer rate for dirty bubbles

Supporting Information:
- Supporting Information S1
- Video clips S1
- Video clips S2
- Video clips S3
- Video clips S4
- Video clips S5
- Video clips S6
- Video clips S7

Correspondence to:
B. Wang,
wanger168@tamu.edu

Citation:
Wang, B., S. A. Socolofsky, J. A. Breier, and J. S. Seewald (2016), Observations of bubbles in natural seep flares at MC 118 and GC 600 using in situ quantitative imaging, *J. Geophys. Res. Oceans*, *121*, 2203–2230, doi:10.1002/2015JC011452.

Received 9 NOV 2015
Accepted 5 MAR 2016
Accepted article online 11 MAR 2016
Published online 2 APR 2016

Abstract This paper reports the results of quantitative imaging using a stereoscopic, high-speed camera system at two natural gas seep sites in the northern Gulf of Mexico during the Gulf Integrated Spill Research G07 cruise in July 2014. The cruise was conducted on the *E/V Nautilus* using the *ROV Hercules* for in situ observation of the seeps as surrogates for the behavior of hydrocarbon bubbles in subsea blowouts. The seeps originated between 890 and 1190 m depth in Mississippi Canyon block 118 and Green Canyon block 600. The imaging system provided qualitative assessment of bubble behavior (e.g., breakup and coalescence) and verified the formation of clathrate hydrate skins on all bubbles above 1.3 m altitude. Quantitative image analysis yielded the bubble size distributions, rise velocity, total gas flux, and void fraction, with most measurements conducted from the seafloor to an altitude of 200 m. Bubble size distributions fit well to lognormal distributions, with median bubble sizes between 3 and 4.5 mm. Measurements of rise velocity fluctuated between two ranges: fast-rising bubbles following helical-type trajectories and bubbles rising about 40% slower following a zig-zag pattern. Rise speed was uncorrelated with hydrate formation, and bubbles following both speeds were observed at both sites. Ship-mounted multibeam sonar provided the flare rise heights, which corresponded closely with the boundary of the hydrate stability zone for the measured gas compositions. The evolution of bubble size with height agreed well with mass transfer rates predicted by equations for dirty bubbles.

1. Introduction

The Deepwater Horizon blowout was the first major oil spill in U.S. deep water and released over 4 million barrels of hydrocarbons to the environment, including up to 1×10^{10} moles of methane, over the span of 83 days [*Kessler et al.*, 2011]. Although limited data were collected inside a 5 km diameter response zone, extensive, new information about the behavior of a deepwater blowout has emerged from this spill. Before the Deepwater Horizon accident, blowout prediction models accounted for the dissolution of gas, but with some uncertainty in the effect of hydrates on the gas dissolution rate, and the dissolution of liquid oil droplets was neglected [*Chen and Yapa*, 2001, 2004; *Johansen*, 2000, 2003; *Yapa and Chen*, 2004; *Yapa and Zheng*, 1997; *Yapa et al.*, 1999; *Zheng and Yapa*, 2000, 2002]. During the Deepwater Horizon accident, a significant intrusion layer formed, centered near 1100 m depth [*Socolofsky et al.*, 2011]. Analysis of observations in the far field for this layer demonstrated that nearly all of the released methane [*Du and Kessler*, 2012; *Kessler et al.*, 2011; *Valentine et al.*, 2010; *Yvon-Lewis et al.*, 2011] and many other higher molecular weight hydrocarbons were partially dissolved from the plume into this intruding water [*Spier et al.*, 2013]. Corresponding measurements in the atmosphere confirmed that all of the methane and a significant fraction of the lighter, liquid components of the oil dissolved subsurface [*Ryerson et al.*, 2011a, 2011b]. However, no measurements were made of the initial bubble or droplet size distribution, an important parameter controlling the rate of dissolution, nor are there direct observations of dissolution in the near-field plume. Hence, models for dissolution in a blowout plume must be validated to other sources of data.

The apparent level of dissolution observed during the Deepwater Horizon accident has an important impact on the predictions of both response-level models, and on impact assessment models. Predictions for transport during a spill are affected by dissolution due to the resulting reduction in the gas bubble and oil droplet size, which reduces the rise velocity. Dissolution also affects assessment of toxicity and biological effects

of the spill by moving some of the more toxic compounds (e.g., benzene) into solution where they remain subsurface and become bioavailable. Yet predicting the dissolution is complicated by the extreme conditions of the deep ocean and the lack of in situ measurements. The purpose of this paper is to analyze quantitative images obtained from direct observation of natural seep bubbles to understand the mechanisms controlling fate (dissolution) and transport (rise velocity) of hydrocarbon bubbles in the ocean environment. These measurements were conducted at two sites in the northern Gulf of Mexico, and the results of these measurements will improve the capability of blowout prediction models as well as increase our understanding of the fate and transport of hydrocarbons released from natural seeps in the oceans.

Conditions controlling hydrate formation and dissolution are similar in a blowout plume in deep water to those in flares of bubbles emanating from natural seeps. Buoyant multiphase plumes from blowouts like the Deepwater Horizon entrain a very large quantity of ambient seawater, which dilutes the rising plume, spreading out the bubbles and oil droplets, and rapidly absorbing the released heat contained in the oil. For example, *Socolofsky et al*. [2011] estimated that on the order of 1000 m^3/s of entrained water entered the 1100 m deep intrusion layer for the Deepwater Horizon spill. *Anderson et al*. [2012] showed that for a wide range of potential blowout types in deep water, the plume quickly cools to near ambient temperatures (within a maximum of 50 m height above the release) and the dissolved gas concentration remains well below the saturation concentration needed for rapid hydrate growth. *Chen and Yapa* [2001] observed similar behavior for a different numerical blowout model with a hydrate kinetics module. Hence, both blowout plumes and natural seep flares will have bubbles and droplets well separated in water with low concentration of dissolved gas at nearly ambient temperature and pressure.

The main difference between a blowout plume and natural seep is the upward velocity of the entrained ambient water and the associated elevated turbulence in a blowout, which are expected to be minimal or absent at a natural seep. Blowout models are well validated for the entrainment velocity [*Yapa et al*., 1999; *Zheng and Yapa*, 2002] and turbulence intensity [*Milgram*, 1983] and consider the entrainment velocity to be additive to the terminal rise velocity of bubbles predicted by empirical equations [*Zheng and Yapa*, 2000]. *Rehder et al*. [2009] showed good agreement between the observed rise velocity of artificially released methane bubbles (similar to natural seeps) and correlation equations in *Clift et al*. [1978]. It is uncertain how the elevated turbulence in a blowout plume may alter the rise velocity or mass transfer of bubbles or droplets in the plume. However, moving in a reference frame of the entrained water, natural seep flares provide a means to observe the role of hydrates, rise velocity, and dissolution rate as they are assumed to occur in the present generation of blowout models.

Observations in the laboratory and the field suggest that hydrates play an important role on the fate of gas bubbles in the oceans. Remote sensing of seep flares using multibeam backscatter data shows that bubbles can survive over long distances from deepwater seeps [*Römer et al*., 2012; *Sahling et al*., 2009; *McGinnis et al*., 2006; *Granin et al*., 2010; *MacDonald et al*., 2002; *Sauter et al*., 2006; *Weber et al*., 2014]. In many cases, these bubbles reach the top of the hydrate stability zone (HSZ) or beyond [*McGinnis et al*., 2006; *Römer et al*., 2012]. Numerical models have been developed to predict the dynamics of individual gas bubbles in seep flares [*McGinnis et al*., 2006; *Römer et al*., 2012]. These models rely on rise velocity and mass transfer rates predicted by empirical equations for bubbles. These models can be validated to direct observations of individual bubbles [e.g., *Rehder et al*., 2009], yet they cannot consistently predict the rise heights of these plumes reported in the literature with a fixed set of calibration parameters [*Römer et al*., 2012]. Hence, the mechanisms responsible for the rise heights observed in the field remain somewhat unknown.

Direct in situ observations of natural seep bubbles in the water column are rare. These observations are important since both the laboratory and field observations of hydrate dynamics show that the surrounding water needs to have an elevated concentration of the hydrate-forming gas before hydrates start to form [*Anderson et al*., 2012; *Warzinski et al*., 2014; *Maini and Bishnoi*, 1981]. *Rehder et al*. [2002, 2009] suggest that saturation concentration existing at the bubble-water interface is adequate to start hydrate formation, and *Rehder et al*. [2009] observed hydrates to form on methane bubbles released artificially into the ocean in the mid water column. Hydrates did not form immediately, and laboratory experiments in a saturated environment also showed a hydrate colonization process which took several minutes in a simulated ocean environment of about 1000 m depth [*Warzinski et al*., 2014]. The few direct observations to date of seep bubbles in the field are by ROV or submersible at the seafloor source, and there is evidence from collected bubbles that hydrate skins do form [*Römer et al*., 2012; *Sahling et al*., 2009], but quantitative measurements

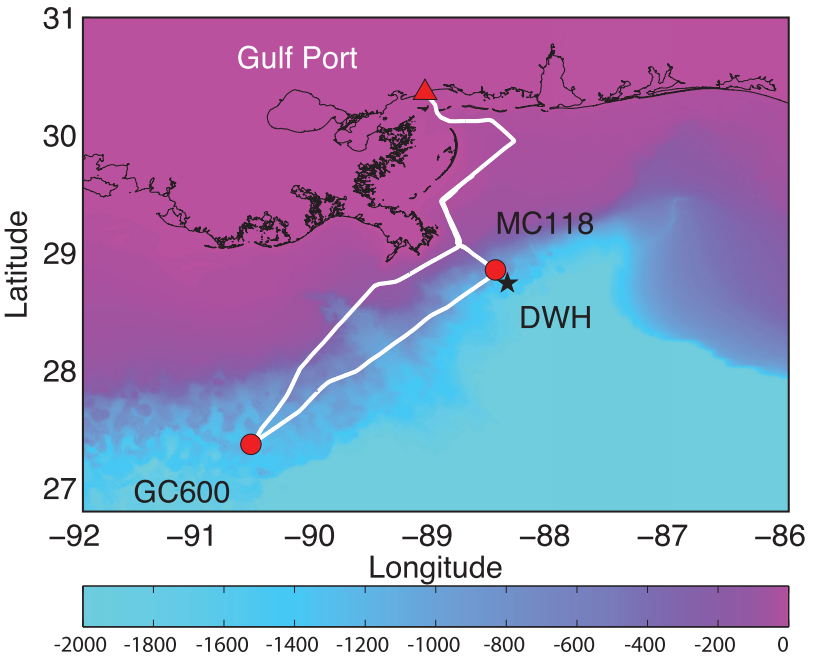

Figure 1. Location of the two main seep sites and the cruise track during the GISR G07 cruise (17–24 July 2014). The location of Deepwater Horizon (DWH) is illustrated for reference. Color bar shows the bathymetry in m from Coastal Relief Models (http://www.ngdc.noaa.gov/mgg/coastal/crm.html).

of dissolution rates for seep bubbles are lacking. Hence, there is a need to verify the formation of hydrate shells on bubbles originating from natural seeps and to track their dissolution by direct observation in the water column.

More observations are available for bubble size distribution and rise velocity from natural seeps. These include direct observation by camera at Coal Oil Point seep field, Santa Barbara (depth less than 100 m) [*Leifer*, 2010], at Vodyanitskii mud volcano, Black Sea (depth of 2070 m) [*Sahling et al*., 2009], at the Makran continental margin (water depth between 575 and 2870 m) [*Römer et al*., 2012], and at GC 185 and GC 234 in the Gulf of Mexico (water depth of 525–550 m) [*Leifer and MacDonald*, 2003]. Among these studies, *Leifer* [2010] carried out a very detailed study and found different size distribution functions to distinguish minor (i.e., low flow rate with narrow size distribution) and major (i.e., higher flow rate with broader size distribution) plumes in shallow water system. Each of these observations has been made with single-camera systems which suffer from parallax error when the magnification of the measurement plane is unknown [*Wang and Socolofsky*, 2015a]. *Greinert et al*. [2006] estimated in situ rise velocities of seep bubbles by tracking the slope of the spatial signal in acoustic data. However, there is no obvious transfer function between acoustic backscatter and bubbles size. Further, none of these studies have quantified the bubble size distribution at significant altitudes above the seafloor, where dissolution rates can be estimated from the shrinkage of bubble size during bubble ascent in the ocean [*Rehder et al*., 2009].

To address some of these observational gaps, we collected gas and water samples and deployed a high-speed stereoscopic imaging system from an ROV to observe seep bubbles and flare dynamics at the seafloor and in the water column for two natural seeps in the northern Gulf of Mexico. In this paper, we focus on the results of the quantitative imaging, and from acoustic measurements. The high-speed cameras allow for visualization of the mobility of the gas-water interface, so that we can see it becomes rigid when a hydrate shell forms [*Warzinski et al*., 2014]. Using two cameras in stereoscopic mode overcomes the parallax problem, allowing for quantification of bubble size and rise velocity over a large observational volume (ideally 0.36 m^3) [*Wang and Socolofsky*, 2015a]. Quantitative measurements are made from the seafloor (between 890 and 1190 m depth) to an altitude of up to 200 m above the source. Section 2 presents a description of the seep sites and measurement and analysis methods, and section 3 reports and discusses the results for observations of hydrate skin formation, bubble size distribution, rise velocity, gas flux measurements, and dissolution rates. The summary and conclusions are given in section 4.

Table 1. Summary of Seep Sites, ROV Dives, and Image Samples

Seep Site	Vent	Category	Location	Dive	Date	Imaging Samples: Bottom	Imaging Samples: Water Column
MC 118	Sleeping Dragon	Primary	28°51.1421′°N 88°29.5109′°W	1–3 (H1350–H1352)	17–21 Jul 2014	22 bursts	8 bursts (20, 50, and 100 m altitude)
GC 600	Confetti	Primary	27°22.1954′°N 90°34.2624′°W	4–6 (H1353–H1356)	21–24 Jul 2014	14 bursts	11 bursts (20, 50, 100, and 200 m altitude)
	Old Reliable	Secondary	27°22.1944′°N 90°34.2635′°W			7 bursts	
	Louie the King	Secondary	27°22.1974′°N 90°34.2596′°W			9 bursts	

2. Methods

2.1. Gas Seep Sites

The Gulf Integrated Spill Research (GISR) G07 research cruise took place during 17–24 July 2014, on the *E/V Nautilus*, using the *ROV Hercules* (operational ROV) and *ROV Argus* (watching ROV) to observe and sample natural gas seeps in the Mississippi Canyon block 118 (MC 118) and Green Canyon block 600 (GC 600). Figure 1 shows the two sites and the cruise track during the G07 cruise along with the location of the Deepwater Horizon blowout for reference. Observations and water column samples were obtained from dedicated instruments mounted on the *ROV Hercules*. The first stage of the survey (dives 1–3) was conducted at Sleeping Dragon vent in MC 118 (28°51.1421′ N 88°29.5109′ W, 17–21 July 2014, water depth 890 m). The second stage of the survey (dives 4–6) took place at a few vents (named during this cruise as Confetti, Old Reliable, and Louie the King) in the Megaplume region of GC 600 (27°22.1954′ N 90°34.2624′ W, 21–24 July 2014, water depth 1190 m). Table 1 summarizes the details of the seep sites, the dives, and the locations where the image data were collected that are presented in this paper.

2.2. Measurement Systems

A wide range of ship-mounted, moored, and ROV-deployed instruments were used to characterize the ambient environment and measure the natural seep vent flares. Ship-mounted instruments included a Kongsberg EM-302 multibeam sonar, which was used to map the sea floor and to detect the seep flares in the water column. To sample the ambient currents, a Nortek up-looking 55 kHz Acoustic Doppler Current Profiler (ADCP) was moored within 2 km of the seep site. The profiler worked properly at MC 118; however, a software malfunction caused the ADCP to shut down during deployment at GC 600. Alternate current data at that site are available from the National Data Buoy Center (NDBC, Station 42369). The ROV carried the remaining measurement packages.

The normal ROV payload of instruments included a CTD (Sea-Bird SBE 49 FastCAT, measuring conductivity, temperature, and depth), five 20 L Niskin bottles mounted vertically on the port side of the ROV, a high-definition primary camera, numerous auxiliary cameras, an ultra-short baseline (USBL) navigation system, and a depth sensor. We also made use of the autopilot capability of the *ROV Hercules*. This system utilizes a rear-mounted Doppler velocity log (DVL) bottom tracking system and sophisticated auto control software. For this cruise, the DVL was a 300 kHz ADCP, which allowed autopilot up to 125 m above the seafloor. This bottom tracking system was capable of stabilizing or moving the vehicle with great accuracy ($\pm$1 cm and $\pm$ 1 cm/s, respectively). Above 125 m altitude, the ROV could be piloted in auto-depth mode using the depth sensor and relying on pilot control for horizontal positioning. To track the flares from the ROV, we added a front-looking M3 Multibeam sonar system (Kongsberg). All of the data recorded by these systems are archived in the Gulf of Mexico Research Initiative Information & Data Cooperative (GRIIDC) [*Socolofsky*, 2015a].

In addition to the CTD and Niskin bottles, two additional systems were interfaced with the ROV for detailed water column sampling. Gas bubbles were collected using isobaric gas-tight (IGT) samplers [*Seewald et al.*, 2002], mounted on the port manipulator arm. Two samplers were used on each dive; both samplers were retrofitted with funnel-shaped bubble collectors. Detailed water samples at selected points in and around the bubble plumes were collected with the SUPR (Suspended Particulate Rosette) sampling system [*Breier*

et al., 2014], which enables fine-scale sampling from remotely operated vehicles. During this cruise, fourteen 2 L bottles were served by the SUPR sampler. Analyses from these two sampling systems are available through GRIIDC [*Breier*, 2015].

Finally, the in situ dynamics and characteristics of individual natural gas seep bubbles were observed using a stereoscopic, high-speed imaging system, TAMU-CAM [*Wang and Socolofsky*, 2015a], which was installed in the front section of the *ROV Hercules*. The system includes two Phantom Miro M340 cameras, each having a full resolution of 2560 × 1600 pixels at 12 bit gray-level intensity and a maximum frame rate of 800 frame-per-second (fps) at full resolution. The cameras were each housed in Prevco pressure housings. Power and Ethernet were provided to the cameras through the ROV umbilical. Lighting utilized the ROV main front lights (two 250 W LED matrix lights, DeepSea Power & Light). An opaque, white backplate was positioned by the port ROV manipulator arm behind the camera field of view to allow for high-quality imaging of the gas bubbles without any background contamination. All images collected by this system and the corresponding metadata are available through GRIIDC [*Socolofsky*, 2015b].

Three ROV dives were conducted at each site resulting in a total of six dives. The general cruise operation consisted of ROV dives with 9–16 h duration, each followed by an 8 h turn-around time during which water column samplers were serviced and multibeam surveys of the seep flares were conducted. More details of the cruise operations can be found in the cruise report [*Socolofsky*, 2015a]. This paper focuses on analysis of the TAMU-CAM images.

2.3. High-Speed Imaging Sampling Locations and Operation

To characterize the behavior of the seep bubble plume, the surveys were initiated at the seep sources on the sea floor and continued up the water column. The M3 Multibeam Echosounder allowed for continuously tracking the seep flare throughout about 600 m of rise above the sea floor. TAMU-CAM samples were collected at the seep sources to characterize potential hydrate formation, the bubble size distribution, rise velocity, and total gas flux, and at several heights in the water column to measure the evolution of bubble size and plume spread. While water samples were collected to nearly the top of the plume, quantitative imaging was limited to altitudes of 200 m or less due to the low void fractions above this height. Seep source measurements were made between 0.5 and 2 m altitude (depending on local bathymetry); quantitative imaging in the water column was measured at 10, 20, 50, 100, and 200 m altitude.

Bubbles were imaged using two different sample modes, named high speed and low speed. During high-speed imaging, sample rates of 200–400 fps were used to visualize deformation of the bubble-water interface on the surface of the bubbles. The objective of this method is to examine the existence and formation of gas hydrate skins similarly to that reported in *Warzinski et al*. [2014]. To measure the bubble size distribution, low-speed imaging was carried out with the sample rates of 24 and 50 fps in order to capture as many independent bubbles as possible with a relatively long, continuous recording time to obtain statistically converged measurements. The image sampling was repeated 2–3 times for each sample location and measurement type (i.e., high or low speed), with each sample, or burst, containing 2020–5776 images. The duration of each burst was 10–28 and 40–240 s for high-speed and low-speed mode, respectively, depending on the selected image resolution and sample rate.

2.4. Image Analysis for Bubble and Flare Characteristics

Quantitative analysis of the TAMU-CAM images was performed for each sample burst using methods based on those utilized in laboratory validation of the TAMU-CAM system, documented in *Wang and Socolofsky* [2015a]. Here we outline the basic approach and highlight any important differences that occur in the field compared to the laboratory.

2.4.1. Qualitative Bubble Behavior

High-speed and low-speed movies of the bubble motion provide direct visual identification of bubble breakup and coalescence, bubble-bubble interaction, bubble-wake interactions, bubble trajectories, and wave motions on the bubble-water interface. As explained in section 2.3, one purpose of the high-speed imaging was to document the mobility of the bubble-water interface, following the method introduced by *Warzinski et al*. [2014]. When the bubble-water interface becomes rigid, this behavior is clearly identifiable in the high-speed movies, and we infer this state to indicate the presence of a clathrate hydrate skin on the bubbles. Several movie clips from the TAMU-CAM system are provided in the supporting information, including clips for each seep source reported here.

2.4.2. Bubble Size Distribution

Low-speed images were analyzed to give quantitative measures of the bubbles sizes for all bubbles in the field of view (FOV) of both cameras. The stereoscopic configuration of the TAMU-CAM system was critical for this and all other quantitative tasks since the variable image magnification can be directly accounted for through stereoscopic positioning. The methods to identify and match individual bubbles between each camera image are described in *Wang and Socolofsky* [2015a] and work well for these flares because the bubbles occurred at a low void fraction.

For the size evaluation, we calculated equivalent spherical bubble diameter using ellipse fitting [*Leifer and MacDonald*, 2003] and area equivalence [*Thomanek et al*., 2010] approaches. Statistically, both approaches provided consistent result in estimating bubble size, but the equivalent bubble diameter computed using ellipse fitting was systematically lower than that computed with the area equivalence method (with ratio of 0.93:1 for our data) [see *Wang and Socolofsky*, 2015b]. In this paper, we report bubble sizes using the area equivalence method. It is noted that the bubbles smaller than 1 mm may be undersampled at in situ camera and lighting configurations. The error associated with such small bubbles may be large as the result of current pixel scale (spanning the range of 0.2–0.3 mm/pixel, depending on the bubble-camera distance).

Probability density functions (PDFs) of bubble size are commonly reported either using the number of bubbles or using the volume of bubbles in each size class as the basis for estimating the probability. Bubble number or population distributions give greater importance to small bubbles than volume distributions, since much of the volume is usually contained in the larger bubbles. Here we report size distributions using population and volume PDFs. For the distribution in population, the observed diameters D were fitted by the following lognormal PDF equation:

$$\mathrm{PDF}=\frac{1}{\sqrt{2\pi}\sigma D}\exp\left(\frac{-(\ln D-\mu)^2}{2\sigma^2}\right) \tag{1}$$

where μ is the mean of the logs of the diameter and σ^2 is the variance of the logs of the diameter. The arithmetic mean λ can be expressed as $\lambda=\exp(\mu+\sigma^2/2)$. For the volume PDF, we replace D by $V=\pi D^3/6$ in equation (1) to fit the PDF and then convert the resulting PDF back to diameter by the inverse of the volume equation. This is equivalent to calculating a volume-weighted distribution of diameters.

We also report a third method called the layer bubble size distribution, defined after *Leifer and MacDonald* [2003] as

$$\Phi=\overline{N/(H\Delta r)} \tag{2}$$

where Δr is the bin width of the bubble radius using logarithmically spaced bins, H is the height of the sample location, and N is the total number of bubbles in each bin. The overbar indicates the averaged value for the entire measurement data set. We used H instead of $H-4r$ in *Leifer and MacDonald* [2003] as $H \gg r$. Similarly, the layer size distribution can be defined with respect to volume, following

$$\Phi_v=\overline{N/(H\Delta r_v)} \tag{3}$$

where Δr_v is bin width of the bubble radius converted from logarithmically distributed volume. From these definitions, Φ and Φ_v describe the bubble size distribution in log-scale per unit vertical distance; hence, these are dimensional scales.

2.4.3. Bubble Rise Velocity

Rise velocity is defined as the vertical component of the bubble speed. Because the rise velocity measurement is sensitive to vehicle motion, rise velocity measurements in this paper are restricted to bursts sampled at the sea floor, where vehicle motion is minimal, as validated by tracking fixed features in the image background. The rise velocity is evaluated by tracking individual bubbles in two consecutive stereo pairs and is given by the vertical distance traveled by the bubble divided by the time interval between image pairs [*Wang and Socolofsky*, 2015a]. This method relies on accurate bubble matching between stereo image pairs and tracking between consecutive images. This method was applied to all bubbles appearing completely in both camera images.

Because not all bubbles appear in both camera images and bubble matching can be challenging, an alternative approach is to calculate the rise velocity from two dimensional tracking in single-camera

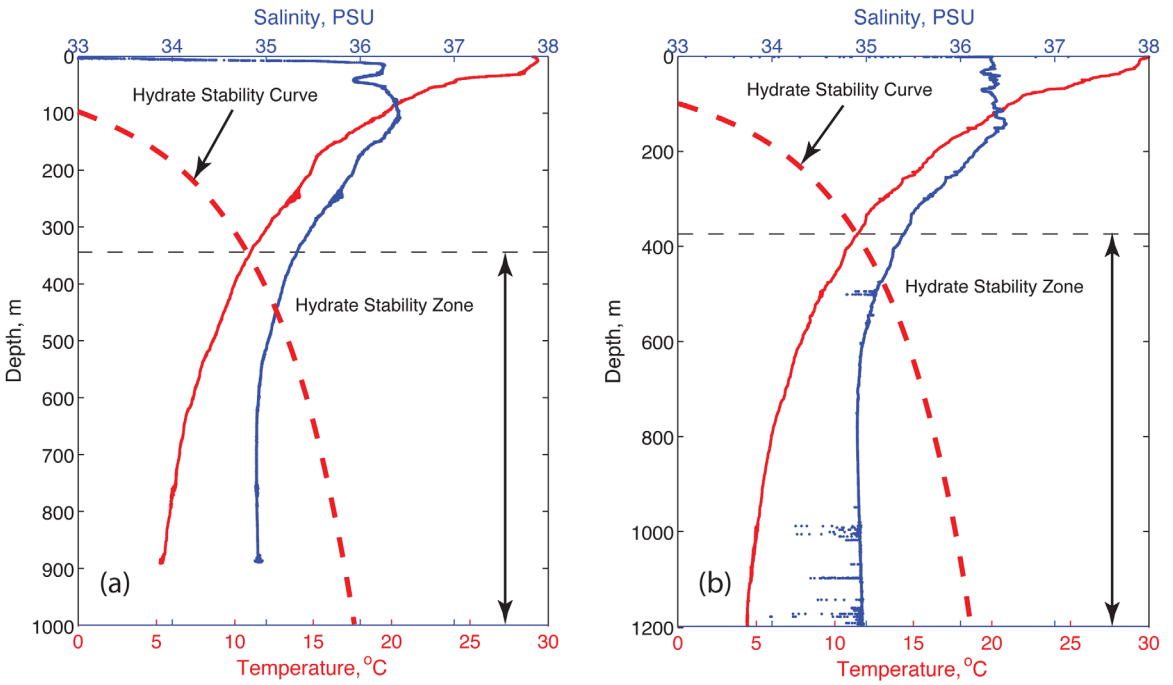

Figure 2. Temperature and salinity profiles at (a) MC 118 and (b) GC 600. The red dashed lines show the hydrate stability curve for the mixture of seep gas calculated with the k_{vsi} method following *Sloan and Koh* [2008] using the Texas A&M Oilspill Calculator, TAMOC [*Socolofsky et al.*, 2015]. The black dashed lines indicate the boundary of the hydrate stability zone.

images. In this method, an averaged pixel scale per image is applied, taken as the average value of the true resolution for all bubbles that are matched in both camera views for a given measurement burst. Our tests have shown that, because the bubble plume is confined to a small region within the camera's depth of field, these two tracking methods render equivalent statistics. Note, however, that the average scale is different in each burst, and the stereo configuration is required to determine this scale.

2.4.4. Vent Gas Flux

Bubble size and rise velocity are two key ingredients for quantification of the total vent gas flux. Here we measure the gas flux by counting bubbles exiting from each flare source and measuring their respective sizes [*Wang and Socolofsky*, 2015a]. For most of the vents, the whole source could be imaged in a single TAMU-CAM system FOV. For the Sleeping Dragon source in MC 118, multiple, overlapping FOVs were required to span the line source of the flare. At that site, we also validated our flux measurements by removing the imaging backplate and counting bubbles from a larger FOV with the seep farther away from the cameras. Although individual bubble sizes could not be estimated from this distance (bubbles were similar in size to a single-camera pixel), the statistics of the bubble size distribution together with the emission counts gave gas fluxes consistent with the overlapping, quantitative FOV bursts.

2.4.5. Flare Bubble Abundance and Void Fraction

As the bubble plume spreads out with height, the space between bubbles increases, and the probability of occurrence of a bubble at a given point in space decreases. We quantify this effect by both counting bubbles and computing the volumetric void fraction. At the seep sources, void fraction is estimated from the volume over which bubbles are measured (i.e., the flare occupies less than the full TAMU-CAM FOV). Above the seafloor, we assume that the FOV of the camera is relatively small compared to the size of the bubble plume in the water column, and we use the full volume of the FOV. Bubble counts are reported in number per volume. The volumetric void fraction is computed as the ratio between the time-averaged total volume of bubbles per image frame and the total sample volume in the image (spanning the range 0.04–0.1 m^3, depending on the selected image resolution). We counted all bubbles in each camera view and took the mean value from the two camera images separately.

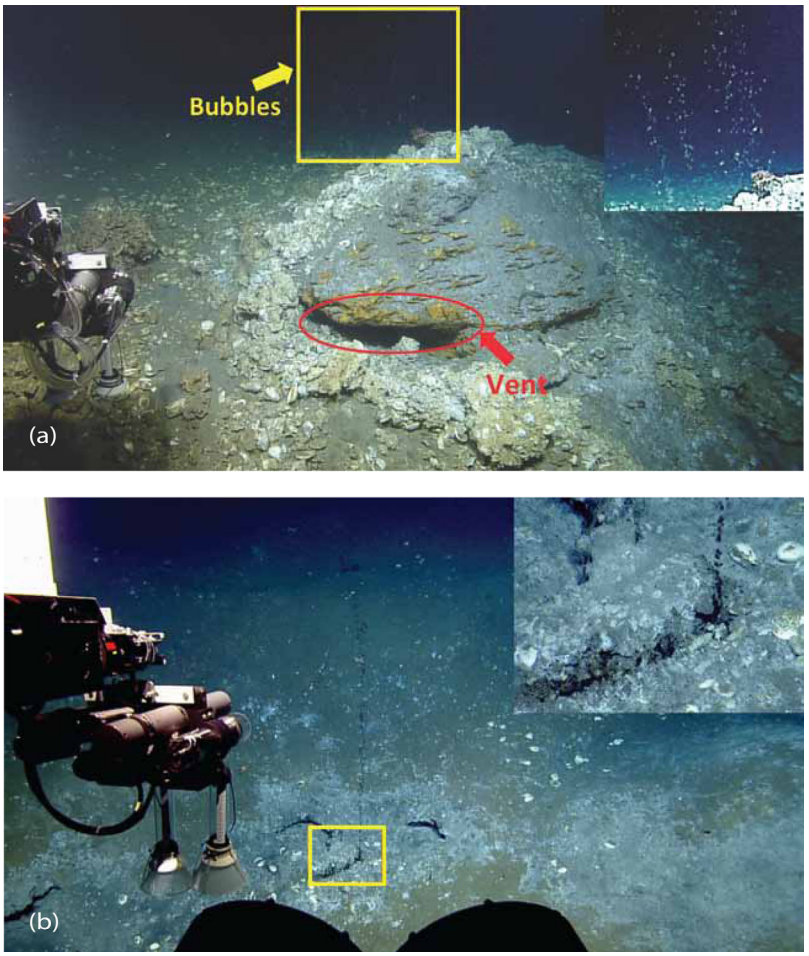

Figure 3. Images of seep sites taken by the HD camera of the *ROV Hercules*. (a) Sleeping Dragon at MC 118. The venting area is highlighted in the red ellipse. The region of the rising bubbles (yellow box) is inserted (enhanced contrast). (b) Confetti plume at GC 600. The area of seep source (yellow box) is inserted. See also supporting information video.

3. Results and Discussion

3.1. Ambient Conditions

Figure 2 shows the profiles of temperature and salinity at both seep sites measured with the CTD on the *ROV Hercules*. The figure also shows the hydrate stability curve, calculated for the measured natural gas composition with the measured ocean salinity and temperature (based on the k_{vsi} method in *Sloan and Koh* [2008], calculated using the Texas A&M Oilspill Calculator, TAMOC [*Socolofsky et al.*, 2015]). The intersection between the hydrate stability curve and the in situ temperature profile defines the pressure boundary of the hydrate stability zone. The ambient temperature and salinity are quite similar for all dives, and the natural gas hydrate should remain stable from the seafloor to approximately 340–380 m water depth.

The ambient velocity data measured by the ADCP indicated that the currents over the entire water column were fairly uniform (between 0.1 and 0.2 m/s) below 100 m and less than 0.1 m/s below 500 m at MC 118. Similarly, the current speed below 600 m at GC 600 was less than 0.1 m/s.

3.2. Characteristics of the Seep Vent Sources

3.2.1. Direct Observation From the ROV

The HD camera installed on the *ROV Hercules* provided detailed color movies of the seep sources and the flares in the water column at both sites. Figure 3 shows example images for the Sleeping Dragon vent in MC 118 and Confetti plume in GC 600. Detailed documentary videos corresponding to this figure are provided in the supporting information (MC 118: S1V1; GC 600: S1V2).

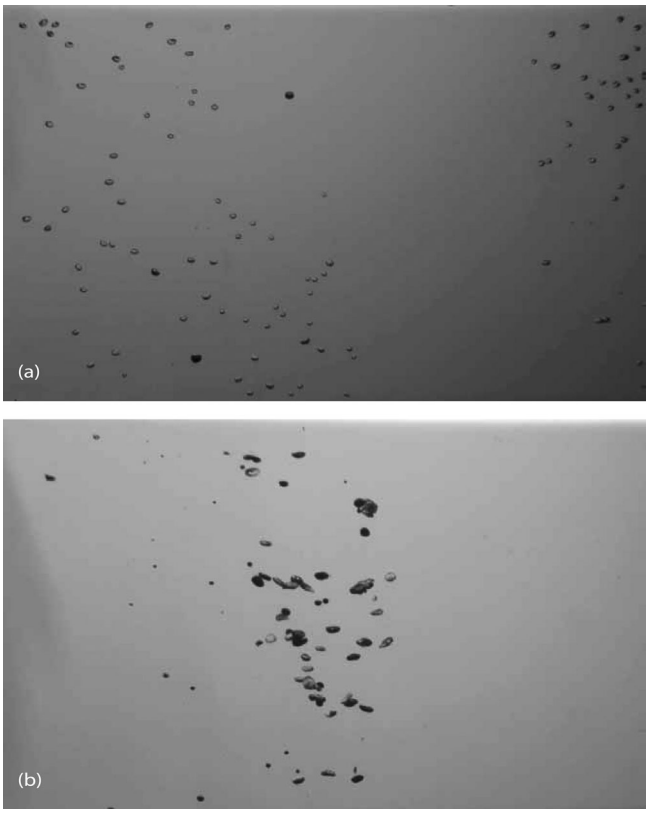

Figure 4. Sample raw images of TAMU-CAM for primary vents at both sites: (a) Sleeping Dragon (MC 118) and (b) Confetti plume (GC 600).

From the direct observation (see supporting information videos), most of the bubbles from Sleeping Dragon are clear (most likely free of oil), escaping from several individual hydrate chimneys (tubes) growing on the vent, each with different releasing frequencies. Some relatively larger and darker bubbles (which may contain oil) are also observed from larger chimneys with much slower frequency to the left in the image. Each tube generates bubbles with an apparently stable release frequency over the measurement period, forming chain-like bubble streams with negligible plume entrainment above each tube. In contrast, the Confetti vent generates much darker bubbles (many likely coated with oil) from a single crack on the seafloor. Because the bubbles leak from a small crack with a relatively fast release rate, the initial flare behavior is more plume-like over the first meter of rise, likely entraining ambient fluid (see Figure 3b).

Figure 4 shows two images from the TAMU-CAM at Sleeping Dragon and Confetti, respectively. These were the primary venting sources during this field investigation. Bubbles are well separated with few overlaps in the image at Sleeping Dragon (see Figure 4a) as the measurement took place about 1.5 m above the seafloor. Bubbles from this vent appear mostly ellipsoidal with the aspect ratio close to unity. This image also shows the clear surface of most of the bubbles. At the Confetti plume, mixtures of clear and dark bubbles are observed (see Figure 4b). Examining the images, the size of bubbles emitted as a group at Confetti are distributed in a wider range compared to the Sleeping Dragon bubbles. The shapes of the bubbles depend on the sizes. The small bubbles are usually spherical, whereas the large bubbles are ellipsoidal or in irregular shapes.

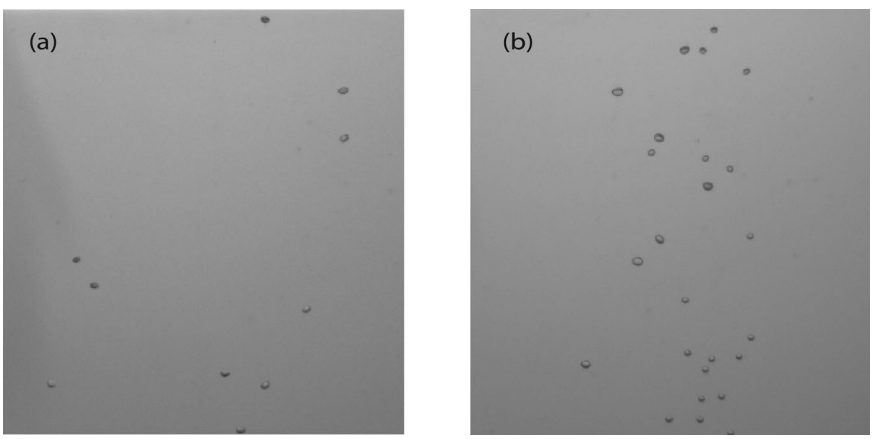

Figure 5. Sample raw images of TAMU-CAM at secondary vents at GC 600: (a) Old Reliable and (b) Louie the King.

Table 2. Gas Composition at the Source[a]

Composition	MC 118	GC 600
Methane	86.28	87.63
Nitrogen	2.68	1.37
Carbon dioxide	1.96	1.90
Ethane	3.35	2.44
Propane	1.51	1.01
iso-Butane	0.30	0.14
n-Butane	0.37	0.35
Neopentane	0.00	0.00
iso-Pentane	0.17	0.09
n-Pentane	0.05	0.06
Total	96.67	94.99

[a]All abundances are in mol %.

In addition to these two primary vents, we measured two secondary seeps at GC 600, which we named Old Reliable and Louie the King. Figure 5 shows sample images for each of these vents. Compared to the Confetti plume, the bubbles appear to be clearer, but with much lower emission rate and smaller, nearly spherical shape.

For a description of the evolution of the shape of these plumes in the water column, refer to sections 3.6.1 and 3.6.2.

3.2.2. Composition of Gas Bubbles

Gas composition at the source for both seep sites was measured from the IGT samples and is summarized in Table 2. The averaged mole fractions of each compositions are reported over all dives. The methane concentration is lower than 99% at both sites, which indicates the sources of these natural seep bubbles are likely thermogenic. These mixtures are also likely similar in nature to those expected during an accidental oil well blowout.

3.2.3. Bubble Behavior Observed by High-Speed Imagery

High-speed imagery confirmed immobilization of the bubble-water interface, consistent with the presence of a hydrate shell on the bubble skin, within 2 m above the source at both sites. This observation relies on many sequential image frames with a very short time interval between frames. Example high-speed videos illustrating the constant bubble shape and interface are provided in the supporting information (S1V3, S1V4, S1V5, and S1V7). Figure 6 also shows several frames of stationary images to demonstrate the irregularity of the frozen bubble shapes during their ascent. These include an irregular-shaped bubble at Sleeping Dragon (Figure 6a), a typical pancake-like shaped bubble at Sleeping Dragon at two different times (Figures 6b and 6c), and an irregular-shaped bubble at Confetti at two different times (Figures 6d and 6e). Many more hydrate bubbles with different sizes and shapes were observed. The shapes of these hydrate bubbles are very similar to those of gas bubbles in the high-pressure water tunnel facility at NETL (National Energy Technology Laboratory) [*Levine et al*., 2015].

The shape of these frozen bubbles influences their rising behavior. Bubbles with pancake-like shape tend to rise with the normal vector of the pancake plane aligned with gravity. At the same time, the bubble body wobbles on a horizontal axis, rocking from side to side. The degree of rotation for each wobble is usually less than 90° with respect to the horizontal plane, and the bubble does not overturn.

The methane concentration in water sampled at each seep source was observed to be at saturation base on the water samples obtained from the SUPR sampler at these seeps. This is a favorable condition for hydrate formation. The observations at the Confetti plume vent allow an estimation of the formation time for the hydrate skin. Due to the bathymetry at the Sleeping Dragon source, the lowest measurement that could be made by the TAMU-CAM was 1.3 m above the release, and all bubbles were observed to have an immobile surface at this height. At the Confetti plume in GC 600, we successfully sampled bubbles with high-speed imagery very close to the seafloor (0.4–0.6 m) and observed mobile gas-water interfaces (see supporting information video, S1V6). We also observed breakup of the larger bubbles into smaller bubbles at this height. This illustrates that hydrate shells have not formed on the Confetti bubbles immediately escaping from the ocean floor. However, the bubbles sampled at 1.4–1.6 m altitude at the same seep during the same dive were found with hydrate shell coating (see supporting information video, S1V7), which indicates that the hydrate shells formed in a short time interval during the free ascent of these bubbles. Based on the rise velocities estimated in section 3.4, the formation time for these hydrate shells observed 1.3 m above Sleeping Dragon and 1.5 m above the Confetti source was between 5 and 10 s.

3.3. Bubble Size Distribution

3.3.1. Primary Vents (Sleeping Dragon and Confetti)

Figure 7 shows the bubble size distribution at the Sleeping Dragon site in MC 118. Measurements for each dive are shown in the plots. Bubble sizes show a consistent peak diameter (diameter with maximum

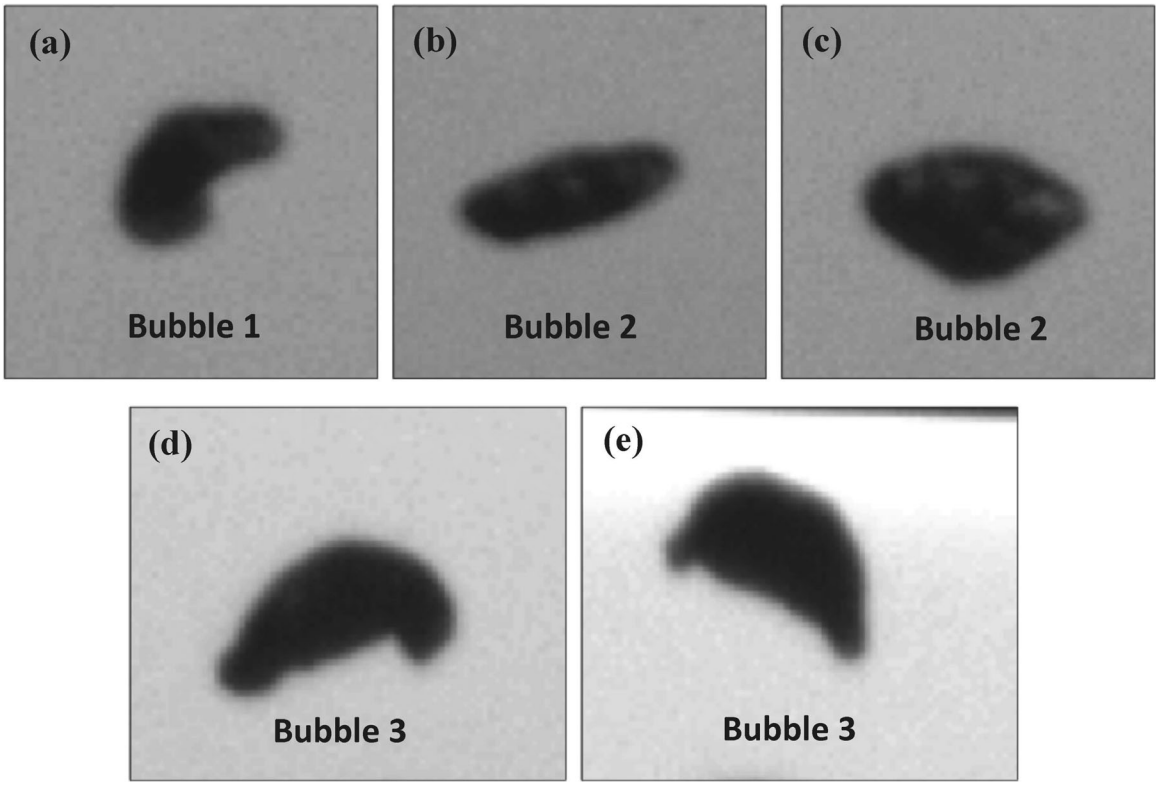

Figure 6. Sample images of bubbles with immobile gas-water interface. (a) An irregular-shaped bubble at Sleeping Dragon; (b, c) the same pancake shaped bubble at Sleeping Dragon for the same viewing angle at two different times; (d, e) the same irregular-shaped bubble at Confetti plume for the same viewing angle at two different times.

probability) in different dives for both population and volume PDFs, and both bubble size distributions show some variability among dives in the tails of the distribution. Due to the very narrow range of bubble size distribution, the shape of the population and volume PDFs is similar, with a larger peak diameter for the volume PDF than for the population PDF. A lognormal function was used to fit all data following equation (1). For the population PDF, we have $\mu = 1.12$ mm and $\sigma = 0.21$ mm with $r^2 = 0.97$. The volume PDF is fit by $\mu = 1.24$ mm, and $\sigma = 0.19$ mm, having $r^2 = 0.98$. According to the lognormal fit, the diameter with maximum probability is 3.2 mm in population and 3.3 mm in volume. The mean bubble diameter and standard deviation calculated from the lognormal fit yield 3.4 and 0.7 mm, whereas our measured data give 3.1 and 0.7 mm. Hence, we conclude that the lognormal distribution is a good representation of our measured data.

The layer bubble size distributions are also shown in Figures 7b and 7d. Similar to the steady plumes reported in *Leifer and MacDonald* [2003], we observe a narrow distribution, showing a power law function in the region above the peak, i.e., $\Phi \sim r^{S_L}$, but with a much larger exponent, $S_L = -8.59$, compared to the values reported in *Leifer and MacDonald* [2003] (which were between -1.62 and -3.1). Our larger exponents indicate a smaller tail to the distribution, hence, a narrower overall bubble size distribution. The region of smaller bubble sizes than the peak can also be described by a power law relation, $\Phi \sim r^{S_L'}$, with the exponent $S_L' = 4.76$ (see Figure 7b). The bubble layer distribution in terms of volume also shows a power law with a clear single peak, but with different exponents than for the population distribution (see Figure 7d). This result is expected due to the characteristic differences between population and volume distributions and was also observed in *Leifer and MacDonald* [2003] but with different power law exponents.

A similar plot to Figure 7 is shown in Figure 8 for Confetti plume bubbles with immobile bubble-water interface. The population PDF shows a relatively flattened peak region (about 2–5 mm), demonstrating a relatively uniform distribution of the bubble sizes in this region. The lognormal fit for all data sets yields a

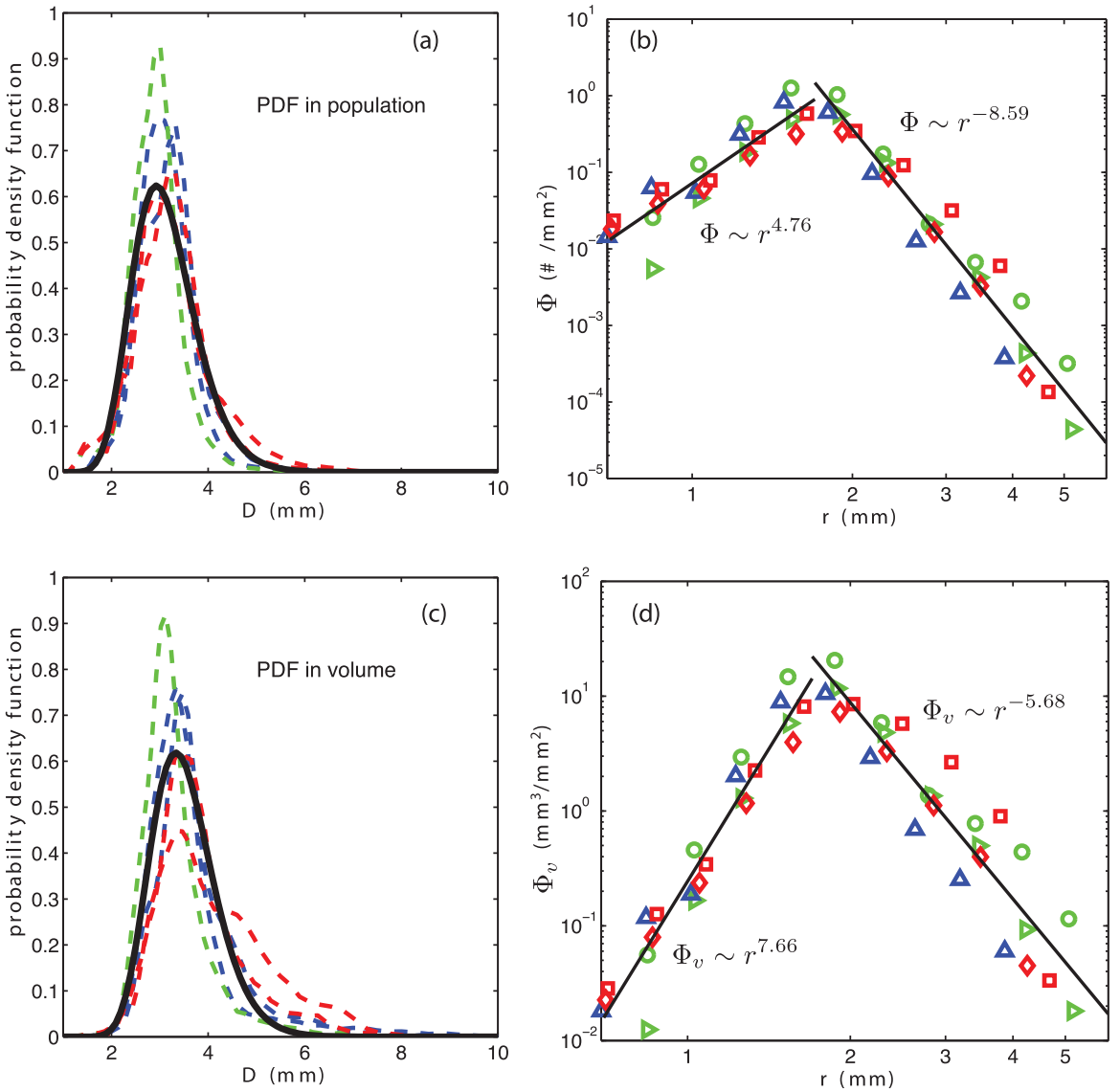

Figure 7. Bubble size distributions at the sea floor for Sleeping Dragon in MC 118. (a) Probability density function of equivalent spherical diameter in population; dashed lines are results for individual bursts where different colors indicate different dives (green, dive 1; blue, dive 2; and red, dive 3) and solid line is lognormal fit to all of the data. (b) Bubble layer size distribution; colors indicate different dives (as in Figure 7a) and the symbols indicate different bursts. (c) Probability density function of equivalent spherical diameter in volume; lines have same definition as Figure 7a. (d) Bubble layer size distribution in volume; data key is same as Figure 7b.

distribution with $\mu = 1.24$ mm and $\sigma = 0.40$ mm (solid line in Figure 8a, $r^2 = 0.95$). This gives a fitted mean bubble diameter of 3.7 mm and standard deviation of 1.6 mm, which correspond well with the measured data (mean = 3.7 mm and standard deviation = 1.4 mm). Comparing to Sleeping Dragon, the size layer distribution also shows a power law dependency but with a milder trend ($S_L = -7.34$ and $S_L' = 1.48$, see Figure 8b). The PDF in volume is plotted in Figure 8c, showing more consistent distributions among different dives comparing to the PDF in population. This is because the contribution of the small bubbles to the total volume is much less than that of large bubbles and most of the variability was observed at the small end of the size range. The best fit lognormal distribution for the volume PDF of bubble diameter has $\mu = 1.67$ mm and $\sigma = 0.27$ mm ($r^2 = 0.96$). The size layer distribution in volume also shows a power law relationship with $S_L = -4.60$ and $S_L' = 4.39$.

In short, all of the measured bubble size distributions at the primary vents can be described by a lognormal distribution, converged over a sampling time scale of 2–4 min. The layer size distribution shows a single peak, indicating a dominate bubble size.

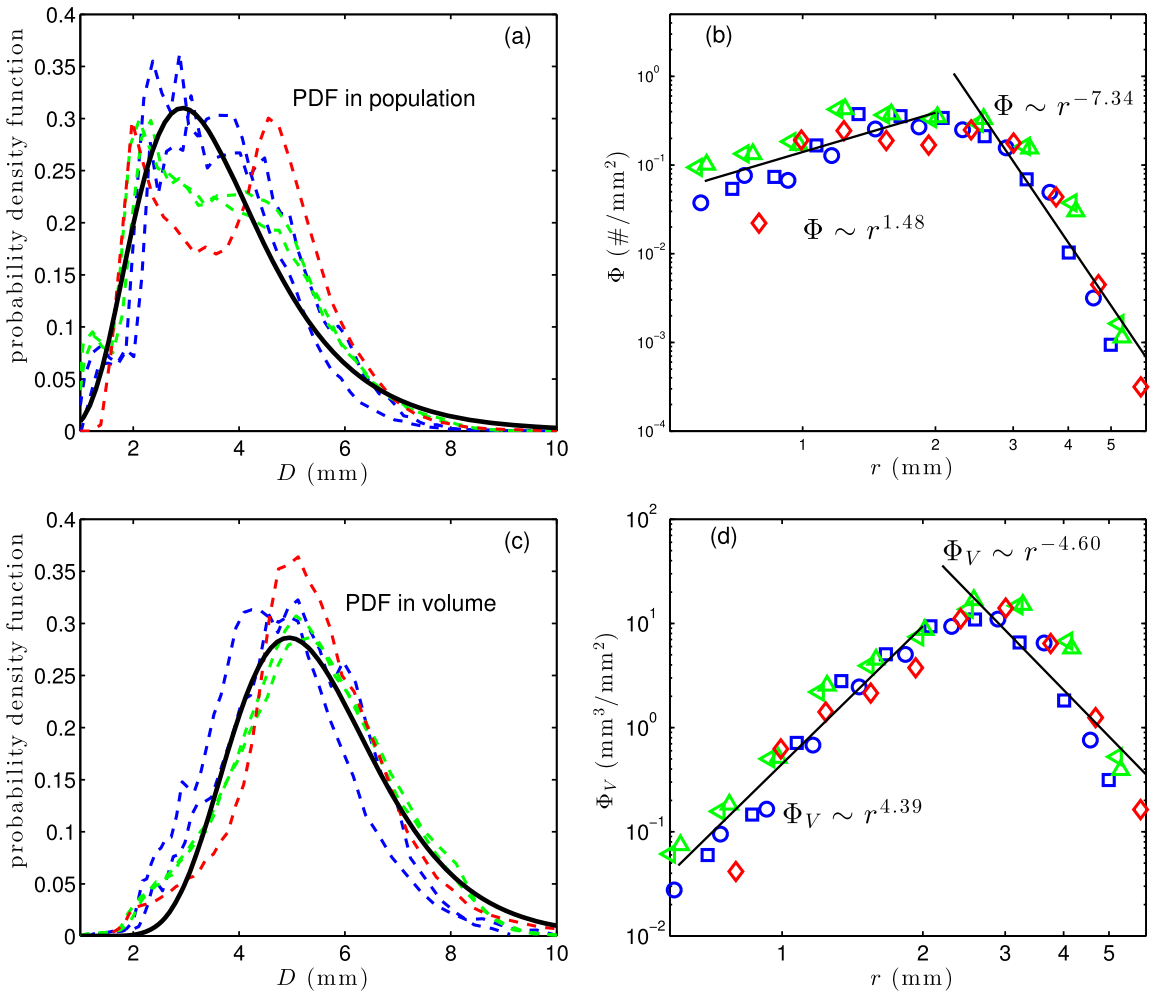

Figure 8. Bubble size distributions at the sea floor for Confetti plume in GC 600 in the same format as Figure 7. Green, dive 4; blue, dive 5; and red, dive 6.

3.3.2. Secondary Vents (Old Reliable and Louie the King)

Figure 9 shows PDF and layer bubble size distributions for Old Reliable in volume only, plotted in a fashion similar to the plots for the primary vents in Figures 7 and 8. In terms of the PDF, different dives (shown in different colors) have relatively diverse size distribution functions but different bursts in each dive (shown in different dashed lines with the same color) usually yield similar distributions (see Figure 9a). This result suggests that the size distribution was changing from dive-to-dive, but statistically stationary over time scales of about 1 h (see further discussion in section 3.3.3). A lognormal distribution was fitted to all of the data for the volume distribution at Old Reliable, yielding $\mu = 1.15$ mm and $\sigma = 0.17$ mm ($r^2 = 0.97$). Very steep slopes of Φ_v in the bubble layer distributions on both sides of the peak suggest the dominant contribution of the bubbles with peak diameter ($D_p = 3.38$ mm). Lognormal and bubble layer distributions were also fitted to the data in population (not shown). The PDF in population is given by $\mu = 0.92$ mm and $\sigma = 0.28$ mm ($r^2 = 0.88$). This gives the fitted mean bubble diameter and standard deviation of 2.6 and 0.7 mm, which are the same as the measured data to one significant figure. Likewise, the bubble layer distribution in populations is fitted by $S_L' = 4.23$ on the rising leg, below a diameter of 2.61 mm, and $S_L = -11.59$ on the falling leg, indicating very few bubbles with diameter greater than the peak diameter.

The other secondary vent, Louie the King, also demonstrates different size distributions at three different dives and similar bubble size distributions in different bursts during the same dive (see Figure 10a). At this vent, small bubbles seem to also be important in the volume distribution. This also affects the plot of Φ_v versus bubble size, which depicts a three-piece power law relationship over the entire bubble size range, a characteristic of a bimodal distribution. Φ_v shows a decreasing trend both at large diameter ($S_L = -6.54$)

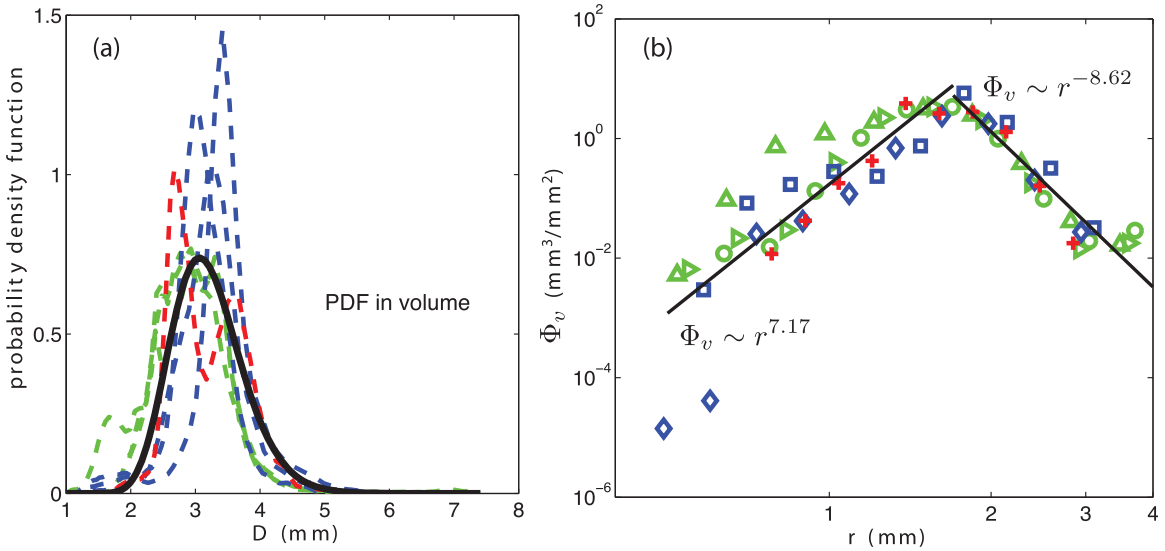

Figure 9. Bubble size distributions at the sea floor for the secondary plume Old Reliable in GC 600. (a) Probability density function of equivalent spherical diameter in volume; dashed lines are results for individual bursts where different colors indicate different dives (green, dive 4; blue, dive 5; and red, dive 6) and solid line is lognormal fit to all of the data. (b) Bubble layer size distribution in volume; colors indicate different dives (as in Figure 9a) and the symbols indicate different bursts.

and at small diameters ($S_L = -2.84$). Between these two negative-slope curves is a steep regime of rising slope ($S'_L = 10.54$). The best fit for the probability density function in volume is given by $\mu = 1.33$ mm, $\sigma = 0.17$ mm, and $r^2 = 0.96$. The distribution in population (not shown) was also analyzed and presents similar characteristics. The lognormal fit for the population probability density function is $\mu = 1.12$ mm, $\sigma = 0.32$ mm, and $r^2 = 0.89$. This gives the fitted mean bubble diameter and standard deviation of 3.2 and 1.1 mm, respectively. These values agree well with the measured data (3.2 and 0.8 mm). Likewise, the bubble layer distribution power laws in population give $S_L = -5.99$ below a diameter of 2 mm, $S_L = -9.30$ above a diameter of 1.8 mm, and $S'_L = 7.40$ between these two critical diameters.

Differently from the primary vents, the bubble size distribution at secondary vents coverages on a time scale of tens of minutes. Despite dive-to-dive variation, the fitted lognormal distributions well describe the bubble sizes. The layer size distributions show the bubble size may have multiple peaks, indicating variation of bubble emission at different dominant sizes. These differences emphasize the fact that these distributions are specific to their measured sites and are not universal distributions.

3.3.3. Temporal Variation

At the secondary vents in GC 600, we observed variation of the seep emission (changing bubble size, population, and flow rate) over short periods of time, which indicates temporal variation of the gas emission. While the flow rate was relatively steady, one or more of the bubble streams could switch from a smaller bubble size (e.g., 1.8 mm diameter) to a stream of larger bubbles (e.g., 2.8 mm diameter) over a time scale of a few seconds. The smaller bubble stream had a much greater number flux in order to maintain the relatively constant observed gas flow rate. Figure 11 shows the bubble streams recorded at the Old Reliable seep at two times separated by 20 s. The emission of small bubbles (shown in Figure 11a) stopped and more large bubbles were present at a later time (see Figure 11b).

We observed this temporal variability only in measurements at the secondary vents during this cruise. Since each burst only lasts for about 3 min, it is not clear whether or not such variability would result in statistically unsteady emission over a longer period. The primary vents seem to have more consistent emission of gas (both in size distribution and flow rate) during the current sampling period (3 days at each site). Because of the hydrate tubes that formed at Sleeping Dragon, the bubble size distribution is narrower than at Confetti plume, where the bubbles emanate from a small crack, originating as large bubbles that break up over the first meter or so of rise.

3.4. Rise Velocity

Rise velocities were computed for individually tracked bubbles for all bursts collected at the seafloor. In general, the measured in situ rise velocities span a large range. Several reasons are responsible for the scattered data in rise velocities. First, the measured rise velocities represent near-instantaneous velocities. These vary

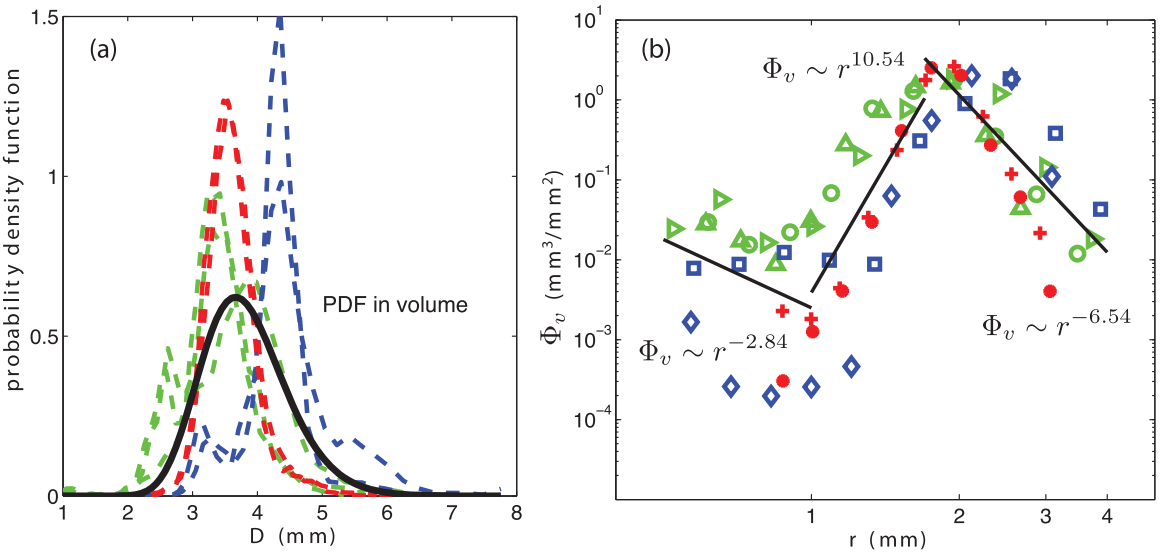

Figure 10. Bubble size distributions at the sea floor for the secondary plume Louie the King in GC 600 in the same format as Figure 9.

due to bubble wobble, local turbulence, local wake-bubble interaction, and time-varying vortex shedding from the bubble-wakes. Second, the estimate contains the measurement error, which is affected by the vehicle motions, the calibration of the stereo setup, and the accuracy of the postprocessing tracking algorithm. Third, individual bubbles have different, irregular shapes, emanate from different parts of the source vent, and may contain different levels of hydrate formation and oil contamination. Finally, very close to the source, rise velocities may be influenced by the plume effect (upwelling velocity of entrained plume water), giving rise velocities that exceed the terminal velocity of a bubble in stagnant water and that vary spatially across the plume. Our error analysis confirms that the first two of these effects are the most significant, with the role of the instantaneous nature of the velocity measurement being the most significant effect explaining the variation of the individual bubble velocity data.

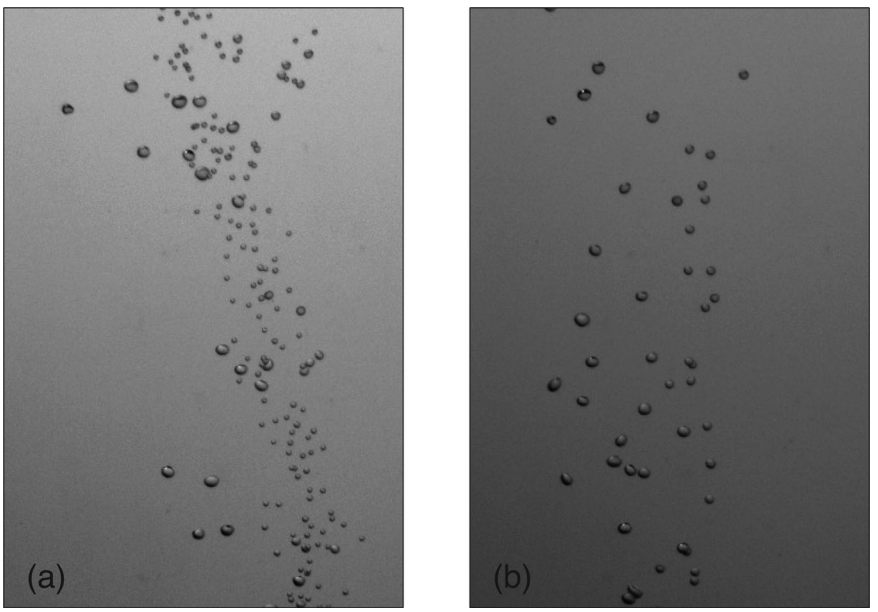

Figure 11. An unstable natural gas emission from Old Reliable vent. (a) A sample image with smaller mean bubble diameter. (b) A sample image with larger mean bubble diameter taken 20 s after Figure 11a during the same measurement burst.

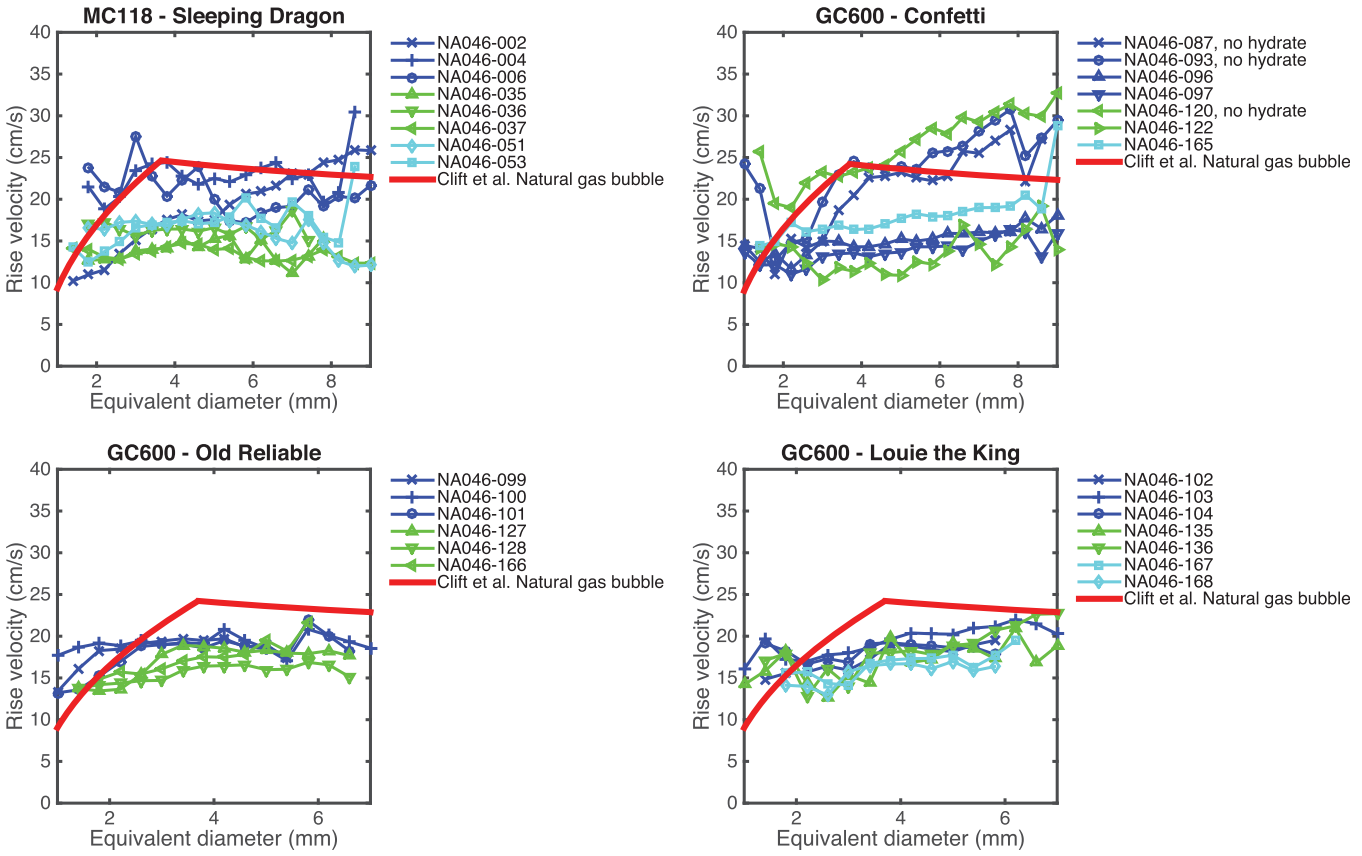

Figure 12. The measured bubble rise velocities for four vents at two seep sites. The calculated terminal velocity of methane bubble under the in situ environment following *Clift et al.* [1978] is plotted for comparison. Different colors indicate different dives. Numbers in the legend give the cruise number (i.e., NA046) and burst sample number (e.g., 002).

Despite the scatter in the instantaneous measurements, the statistics of rise velocity as a function of bubble size are well converged and show consistent trends among bursts and across each of the dives. Figure 12 presents the mean values for rise velocity computed for each image burst, averaged in bins of equivalent spherical bubble diameter between 1 and 9 mm with bin sizes of 0.4 mm. It should be noted that most of the measured bubble rise velocities are expected to be their terminal velocities under this low void fraction condition. Because the bubbles were observed to have an immobile interface, we expect their terminal rise velocity to correspond to dirty bubbles. The red line in the figure shows the empirical prediction for dirty bubble terminal velocity from *Clift et al.* [1978], computed using the in situ natural gas bubble properties. Bubble properties were computed using TAMOC as follows: density $\rho_p = 88.2$ kg/m^3 at 890 m at MC 118, $\rho_p = 126$ kg/m^3 at 1190 m at GC 600 and surface tension $\sigma_p = 0.061$ N/m at both sites [*Sachs and Meyn*, 1995]. The rising part of the curve for bubble sizes below 3 mm corresponds to spherical-shaped bubbles; the flatter relationship between 3 and 9 mm is for ellipsoidal bubbles.

At MC 118, the rise velocities in two of the bursts (NA046-004 and NA046-006) track closely to the *Clift et al.* [1978] empirical equations line, with the data in the remaining bursts grouping about 40% lower than the empirical line over the size range from 3 to 9 mm. Each measured curve in the figure is for a single imaging burst, which covered a duration of a few seconds up to 2 min, depending on the TAMU-CAM frame rate. Hence, each measurement gives the bubble behavior during a short time window. Also, at MC 118, all of the observed bubbles had immobile interfaces at the measured heights.

Similar behavior is observed for GC 600, but perhaps for different reasons. The bubble rise velocities in three of the measurement bursts approach or exceed the *Clift et al.* [1978] empirical fit line (NA046-087, NA046-093, and NA046-120), and the rise velocities of the remaining measurement bursts fall about 40% below the empirical line. The three data sets at GC 600 that track the empirical line were all measured very close to the seafloor. Bubbles in these data were observed to have mobile interfaces (incomplete hydrate

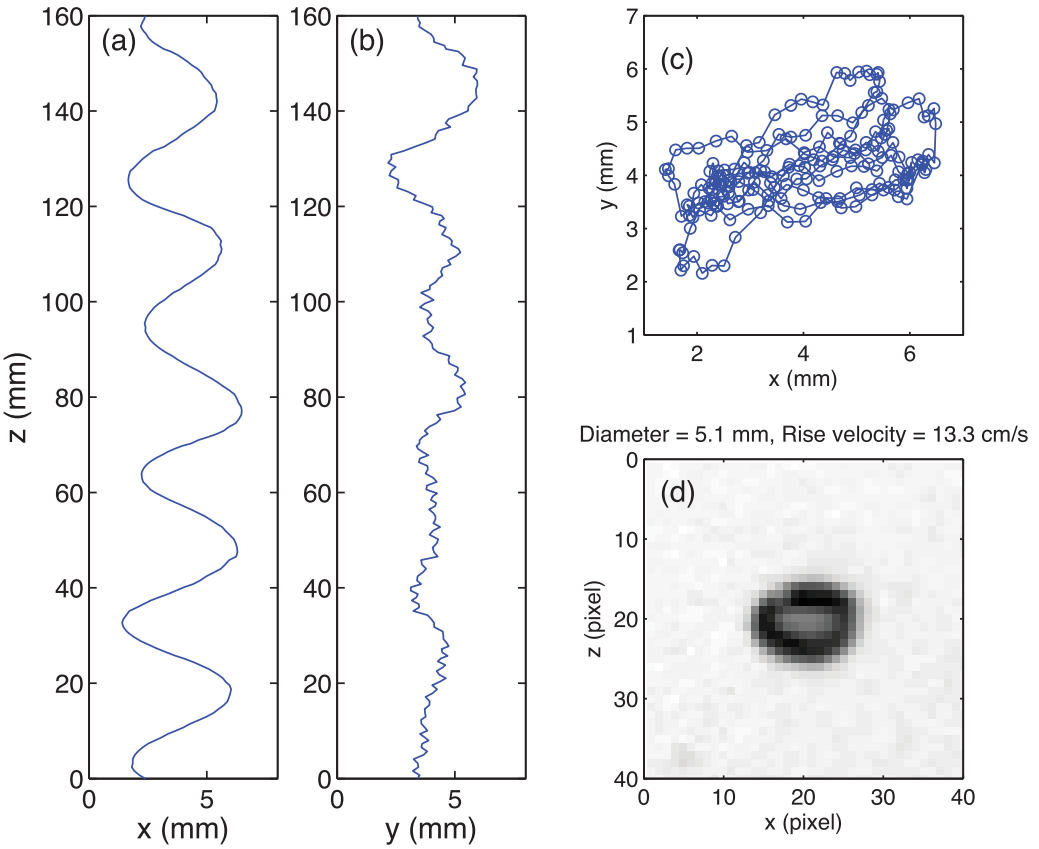

Figure 13. The trajectory of a near zig-zag rising bubble. The *x* and *y* coordinate system is moving in the reference frame of the mean currents; *z* is fixed relative to the stationary ROV. (a) *x*–*z* plane. (b) *y*–*z* plane. (c) *x*–*y* plane (i.e., plan view). (d) Bubble image.

formation). We also noted strong bubble-wake interaction due to the tight width of the plume. Hence, these higher velocities were for nonhydrated bubbles and may include an upwelling velocity from the plume effect. All of the measurements with slower rise velocities were taken about 1.5 m higher in the water column, where the bubble interfaces were observed to be immobilized (indicating hydrate formation), and where the plume effect had dissipated due to the ambient currents stripping away the entrained fluid. At the two secondary seep sites, all of the bubbles were observed to have immobile surfaces, and the plumes were diffuse, showing no plume effect. The measurements at each of these secondary plumes are close to the lower velocity measurements at the primary seep sites.

These data support the conclusion that there are two potential rise velocities for bubbles in the ellipsoidal shape regime: a slower velocity about 40% below the empirical prediction from *Clift et al*. [1978] and a higher velocity that closely tracks the *Clift et al*. [1978] line. There is some indication that hydrate formation plays a role in which velocity will be exhibited by a bubble (i.e., all fast bubbles measured at GC 600 were in a no-hydrate regime), but hydrated bubbles at MC 118 occasionally tracked the faster velocities.

Laboratory experiments have previously reported this two-mode rise velocity, and correlated these two velocities with the trajectory of the bubble path in the water column [*Wu and Gharib*, 2002; *Tomiyama et al*., 2002]. In the *Wu and Gharib* [2002] experiments, faster bubbles follow a helical path, and slower bubbles follow a zig-zag path, restricted to a narrow two-dimensional plane. Previous authors showed that initial shape deformation during bubble formation can trigger the helical or zig-zag path, and that once the bubble starts to follow one of these two trajectories, it seems to maintain that trajectory [*Wu and Gharib*, 2002; *Tomiyama et al*., 2002; *Laqua et al*., 2016]. There are, however, no theories to predict the initial shape deformation for simple orifice-type sources, and the rise velocity appear to be random with no underlying structure to the statistics. *Tomiyama et al*. [2002] also show that while all zig-zag bubbles followed a slower rise

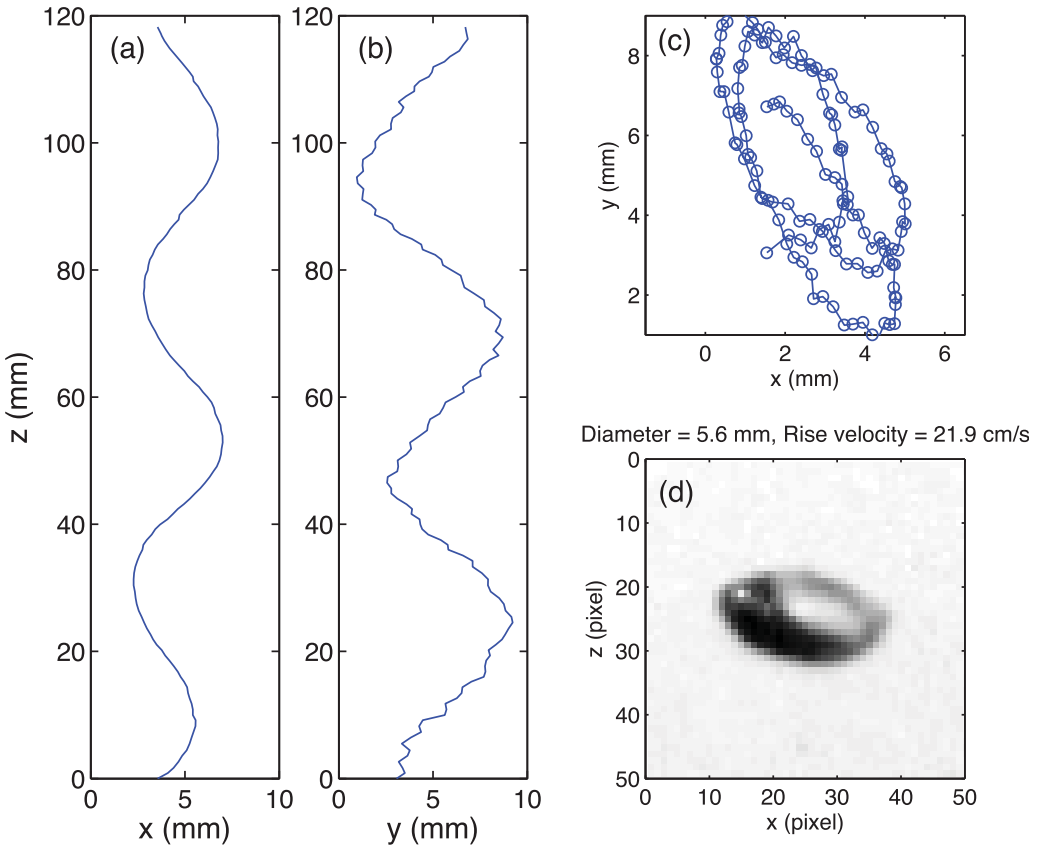

Figure 14. The trajectory of a near helical path rising bubble. The *x* and *y* coordinate system is moving in the reference frame of the mean currents; *z* is fixed relative to the stationary ROV. (a) *x*–*z* plane. (b) *y*–*z* plane. (c) *x*–*y* plane (i.e., plan view). (d) Bubble image (note the bubble in this image is closer to the ROV, yielding a greater magnification than the bubble in Figure 13).

velocity in their experiments, bubbles following a helical path can range in rise velocity from the *Clift et al.* [1978] equation line to as slow as the zig-zag rise velocity. Hence, slower bubbles may be correlated either with zig-zag path trajectories or with slower helical paths.

We tested our data for this behavior using the stereoscopic capability of the TAMU-CAM system. Figure 13 shows the trajectory of a 5.1 mm equivalent spherical diameter bubble in three-dimensional space. The coordinate system is oriented with *z* positive upward. To obtain the trajectory, the bubble is tracked, then the mean *xy*-translation of the bubble over the rise through the sample volume is removed from the bubble motion. This subtracts out the mean currents, leaving the trajectory as if the bubble rose in a stagnant tank. The plan view plot in *xy* space shows that the bubble follows quite closely the zig-zag pattern, with a maximum excursion of about 5 mm along the long axis of motion and about 1 mm along the short axis, giving an aspect ratio of 5:1. Note that this is the trajectory of the center of the bubble. This bubble rising along this zig-zag path had a rise velocity of 13.3 cm/s over the measurement interval, consistent with the slow rise velocities measured at these seeps.

Figure 14 shows the trajectory of a 5.6 mm equivalent spherical diameter bubble, which follows closer to a helical rise path. The maximum excursion of this bubble is 8.9 mm along the long axis and 4 mm along the short axis, giving an aspect ratio of 2:1. The rise velocity for this bubble was measured as 21.9 cm/s over the measurement interval, 40% greater than the velocity of the bubble in Figure 13 despite the fact that they have very similar equivalent diameters. This behavior appears to be consistent across our measurements: faster-rising bubbles are correlated with helical rise paths. Hence, our rise velocity data are consistent with the literature and support the conclusions that most of the bubbles measured at these vents during these dives followed a slower, zig-zag trajectory. These data are also consistent with recent high-pressure tests of methane bubbles in a simulated deep-ocean environment [*Laqua et al.*, 2016].

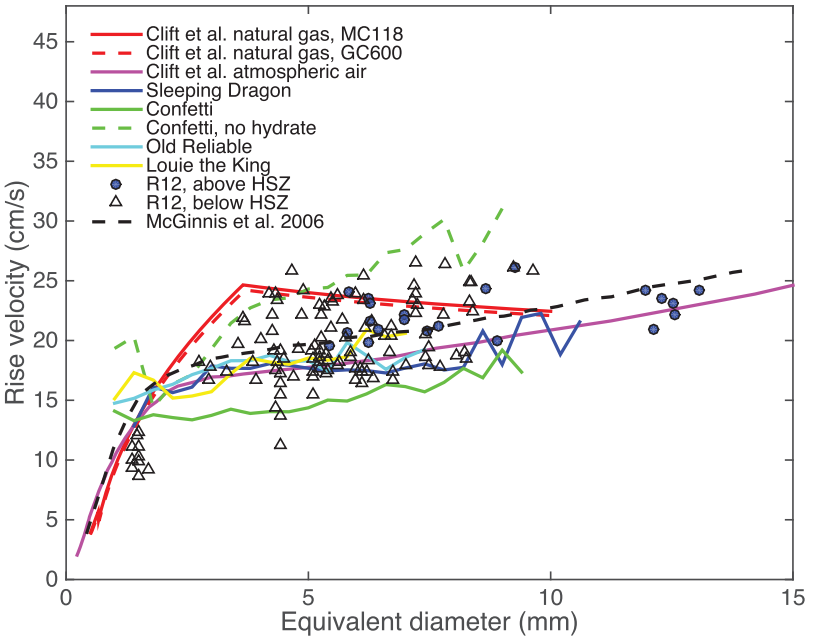

Figure 15. Measured rise velocity versus equivalent spherical bubble diameter. The in situ methane bubble terminal velocity (red line) was calculated using empirical equations in *Clift et al*. [1978]. The hand-drawn curve for dirty air bubbles at standard conditions (purple line) is digitized from *Clift et al*. [1978, Figure 7.3]. The measurement data of *Römer et al*. [2012] were digitized and reproduced from their Figure 14. Their data are regrouped into two categories (seep sources above the HSZ marked as "R12, above HSZ" and seep sources below the HSZ marked as "R12, below HSZ"). The prediction of McGinnis et al. [2006] (black dashed line) was also digitized from *Römer et al*. [2012, Figure 14].

All of our rise velocity data are summarized with selected, representative data from the literature in Figure 15. Literature data include data from *Römer et al*. [2012], and *McGinnis et al*. [2006]. The data in *Römer et al*. [2012] are digitized from their Figure 14 and grouped into seep sources that were above the hydrate stability zone (flares 2, 5, and 6 in their paper) and sources from below the hydrate stability zone (flares 1 and 15 in their paper). The rise velocity curve from McGinnis et al. [2006] is a prediction using different empirical equations; this curve was also digitized from *Römer et al*. [2012, Figure 14]. One additional correlation line is presented in the figure, called *Clift et al*. [1978] atmospheric air in the legend. This line is a hand-drawn correlation line presented in *Clift et al*. [1978, Figure 7.3], which is intended to give the lower bound of measured values for air bubbles in water at atmospheric pressure. This correlation is the one most often used in papers reporting natural seep data that reference *Clift et al*. [1978], and we emphasize here that this line is not that given by the empirical equations in that reference (the empirical equations give the red lines in our figures).

Comparing to these other studies, our measured data show similar trends. The rise velocity data from *Römer et al*. [2012] span a similar range to our data, and there is no consistent trend between sources above or below the hydrate stability zone for their data. We also measured hydrated bubbles with fast and slow rise velocities, in agreement with that finding. The majority of our measured data coincidentally track the lower line from the *Clift et al*. [1978, Figure 7.3], which is the lower bound for terminal rise velocity of an air bubble. The curve from McGinnis et al. [2006] is slightly higher than the curve of *Clift et al*. [1978] and agrees well with our data. We have shown evidence that this lower rise velocity is most likely correlated with a zig-zag trajectory. Hence, our conclusion is that natural seep bubbles can follow faster, helical path trajectories, and slower, zig-zag trajectories, and that there appears to be a preference for the slower rise velocity for the data measured in our study.

3.5. Gas Flux

Gas fluxes were estimated from each measurement bursts collected at the sea floor and are reported in Table 3.

Table 3. Seep Flow Rate Estimates for Individual Imaging Bursts

Vent	Dive	Burst	D_{50} (mm)	Median Bubble Diameter (mm)	Gas Flux (L/min)
Sleeping Dragon (MC 118)	H1350 (dive 1)	NA046-004	3.7	3.2	0.08
		NA046-005	3.6	3.2	0.13
		NA046-007	3.3	3.1	0.06
		NA046-015[a]	3.2	3.0	0.19
		NA046-018[a]	3.2	3.0	0.22
	H1351 (dive 2)	NA046-034	3.3	3.1	0.15
		NA046-035	3.2	3.0	0.08
		NA046-036	3.4	3.1	0.11
		NA046-037	3.1	2.9	0.09
	H1352 (dive 3)	NA046-052	3.8	3.2	0.08
		NA046-058	3.8	3.2	0.10
Confetti (GC 600)	H1353 (dive 4)	NA046-086	4.6	3.4	0.17
		NA046-087	5.0	3.7	0.16
	H1354 (dive 5)	NA046-123	5.2	3.6	0.16
		NA046-124	5.2	3.5	0.15
	H1355 (dive 6)	NA046-165	5.2	4.1	0.23
Old Reliable (GC 600)	H1353 (dive 4)	NA046-100	2.9	2.6	0.03
		NA046-101	2.5	2.1	0.03
	H1354 (dive 5)	NA046-128	3.3	3.1	0.02
		NA046-132	3.0	2.8	0.02
	H1355 (dive 6)	NA046-166	3.1	2.7	0.02
Louie the King (GC 600)	H1353 (dive 4)	NA046-103	3.7	3.1	0.02
		NA046-104	3.3	3.0	0.02
	H1354 (dive 5)	NA046-136	4.2	4.1	0.01
		NA046-137	4.3	4.2	0.02
	H1355 (dive 6)	NA046-167	3.6	3.5	0.01
		NA046-168	3.5	3.4	0.01

[a]For theses bursts, the full bubble population from the Sleeping Dragon seep was imaged in a single-camera FOV without the back plate, and the bubble sizes were calibrated using the measurement results from the images with the back plate.

At Sleeping Dragon, the seep source was along a line larger than the FOV of the TAMU-CAM system; hence, measurements with the backplate spanned only part of the plume. For each of these partial measurements, we used to ROV HD camera to estimate the fraction of the full vent flux captured by the measurement. We then collected multiple, overlapping measurements to estimate the total gas flux. The flux estimated using this approach was 0.2–0.3 L/min. The two measurements with the backplate removed were able to span the full source width in a single FOV. These were samples NA046-015 and NA046-018, and the flux estimated from those samples ranged from 0.19 to 0.22 L/min.

For Confetti vent, almost the entire population of bubbles was emitted from a single source; therefore, we were able to measure the total gas volume flux from each individual burst (see Table 3). From 3 days' surveying (dives 4–6), the calculated gas flux was between 0.15 and 0.23 L/min. Because many of the bubbles at Confetti appeared to be dark in the image, it was difficult to identify the sizes of individual bubbles where bubbles were overlapping in the image. We estimated that 10% of the overlapped bubbles were falsely identified as a single bubble signature. These false identifications lead to overestimation of the flow rate when the computed volume for the group is more than the sum of the individual bubble volumes (e.g., when bubbles appear side-by-side) and result in underestimation when the computed volume is less than the sum of the individual bubble volumes (e.g., when bubble pass behind each other). Considering this two-way influence, we expect the overlapping does not lead to significant error to the estimation of the overall gas flux. This was also confirmed, but with a lower percentage of false identification, in corresponding laboratory experiments [*Wang and Socolofsky*, 2015a].

For the other two secondary vents, the gas flux is much less. The bubble images are clear and bubbles are well separated in the images. The estimated gas fluxes for Old Reliable and Louie the King vents were 0.028 ± 0.006 and 0.013 ± 0.004 L/min, respectively.

3.6. Vertical Profile of Flare Properties

3.6.1. Physical Properties of the Flares

As the flares were tracked up the water column, quantitative imaging was applied up to altitudes of 200 m above the seafloor. Due to the difficulty for the ROV camera to track these small bubbles in the mid water

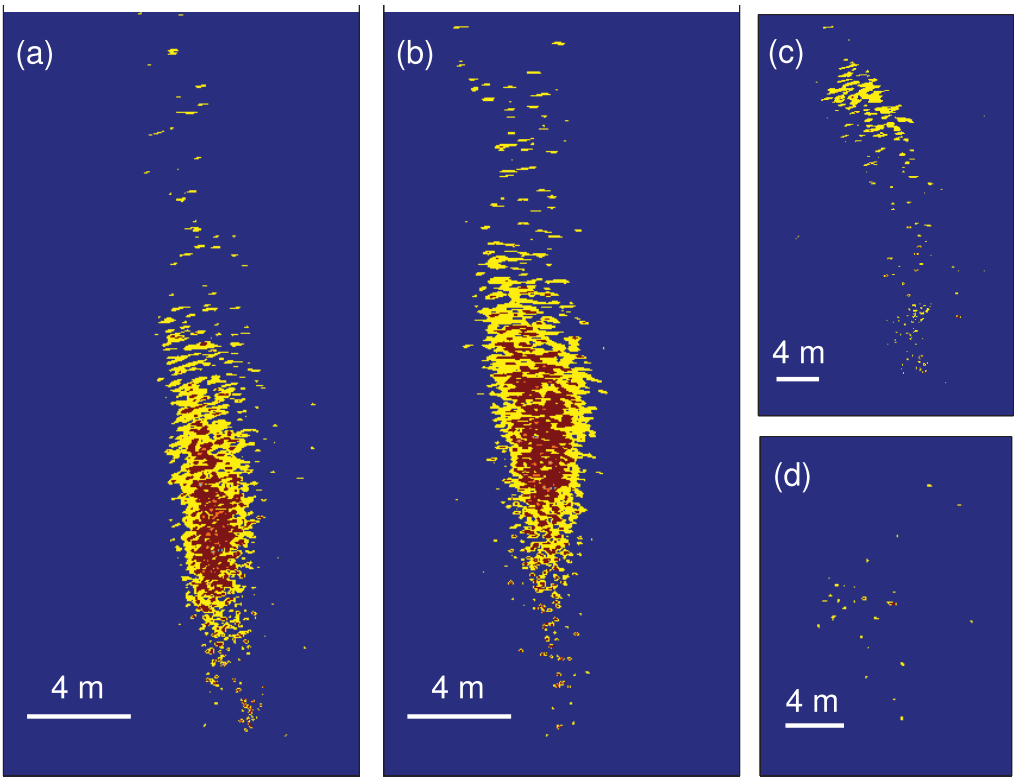

Figure 16. Cross-sectional plume signal at different altitudes for the Sleeping Dragon seep at MC 118 measured by the M3 multibeam sonar: (a) 10 m; (b) 20 m; (c) 50 m; (d) 100 m.

column under the current lighting condition, a forward-looking M3 sonar was used as a reliable method to track the flares. Currents have the effect of stretching out the plumes, with faster-rising bubbles in the upstream region, and slower-rising bubble trailing downstream; a sequence of random motions, due to ocean background turbulence, random-directed secondary currents, and bubble rising trajectories, spreads the plumes laterally a much shorter distance than in the main current direction. Figure 16 shows the plume cross-sectional profile recorded by the M3 sonar for the Sleeping Dragon vent at 10, 20, 50, and 100 m above the sea floor. Water column sampling and quantitative imaging were both done by positioning the ROV at the center of the region giving the largest amplitude (red color in the figure) in the M3 sonar signal. This location is where the bubbles are the most abundant and is generally about a third of the way between the fastest upstream bubbles and slowest downstream bubbles visible to the M3 sonar.

Figure 17 shows a comparison of the M3 sonar signature at the two sites at an altitude of 10 m. Because the Sleeping Dragon vent was the only major vent in its vicinity, the signal at MC 118 gives a single plume. At GC 600, the three vents were in close proximity, and usually all three vents could be seen in the M3 sonar view. Figure 17b shows the Confetti vent toward the bottom of the figure and the Old Reliable (left) and Louie the King (right) vents as the two larger returns in the upper quarter of the figure. Moving up the water column, when the currents are aligned with the line connecting the vents (as they are here for Confetti and Old Reliable) the plumes merge shortly above the bottom. In this orientation of the currents, Louie the King remains independent and does not merge. Because the source flux from the Confetti vent was much greater, most of the bubbles in the main M3 sonar return region where sampling was conducted originated at the Confetti vent.

The fractionation, or sorting, by the currents and the lateral spreading of the plume by random motions both work to dilute the concentration of bubbles in the flares with height. Figure 18 illustrates the profiles of the number of bubbles per cubic meter and volumetric void fraction as a function of height above each vent. Both of these quantities exhibit a power law dependence on height, with the decay following $\sim z^{-0.75}$ for the bubble abundance and $\sim z^{-0.79}$ for the volumetric void fraction. Each of these values was measured

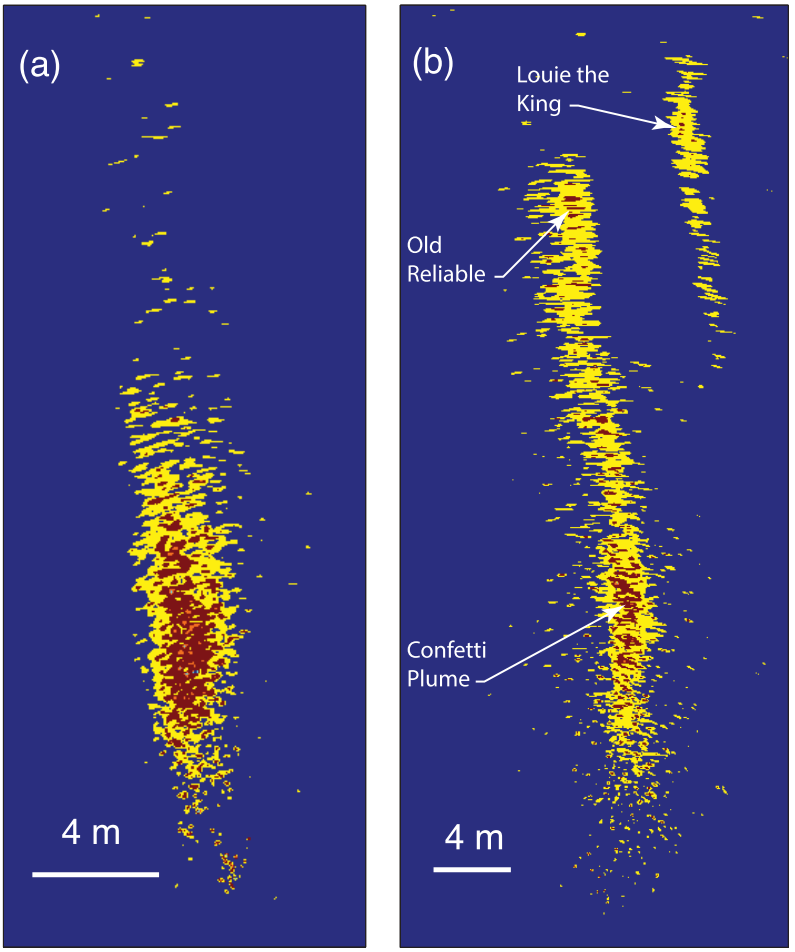

Figure 17. Cross-sectional plume single at 10 m altitude for different seeps. (a) Sleeping Dragon in MC 118 and (b) Confetti (large signal) and Old Reliable (weaker signal) in GC 600.

by the TAMU-CAM. Quantitative analysis of the M3 sonar signature itself also gives the evolution of the plume. Its dilution is seen in the increase of its width (minor axis of the plume in Figures 16 and 17). The plume width 2*b* expands with height, showing a much slower growth rate than that would be expected for plume that is entraining ambient water [*Fischer et al*., 1979]. Hence, these results support the model of the vent flare lacking entrained water, absent of a significant upwelling flow. This behavior is expected for a weak plume in crossflow [*Socolofsky and Adams*, 2002].

3.6.2. Flare Height-of-Rise From Multibeam Data

The ship-mounted multibeam sonar provided a coarse-resolution mapping of the seep flares at these sites. The multibeam measurement is made by mapping the hydroacoustic anomalies recorded in the backscatter signal from the sonar. Figure 19 shows the result for all survey passes at each site. Surveys were conducted by moving the *E/V Nautilus* along a grid pattern over the seep sources. Typical grid spacing was on the order of 250–500 m along tracks about 2–3 km long; tracks were surveyed both east-west and north-south trending. The grid mapping was repeated several times during the period between ROV dives. The top of each flare is clearly identifiable in the multibeam data, and similar results have been reported for these and other seeps in the literature [*Römer et al*., 2012; *Granin et al*., 2010; *Greinert et al*., 2006; *McGinnis et al*., 2006].

From these data, the height-of-rise of these bubbles was 490 m for MC 118 and 840 m for GC 600. These correspond to depths of 400 m at MC 118 and 350 m at GC 600. Both anomalies indicate that the bubbles survived to a height very close to the boundary of the HSZ (around water depth of 340–380 m depth, shown in Figure 2). The deeper seep is capable of rising to a similar depth due to the higher density of the gas (hence, a larger mass of methane is contained in the same bubble size at GC 600 compared to MC 118)

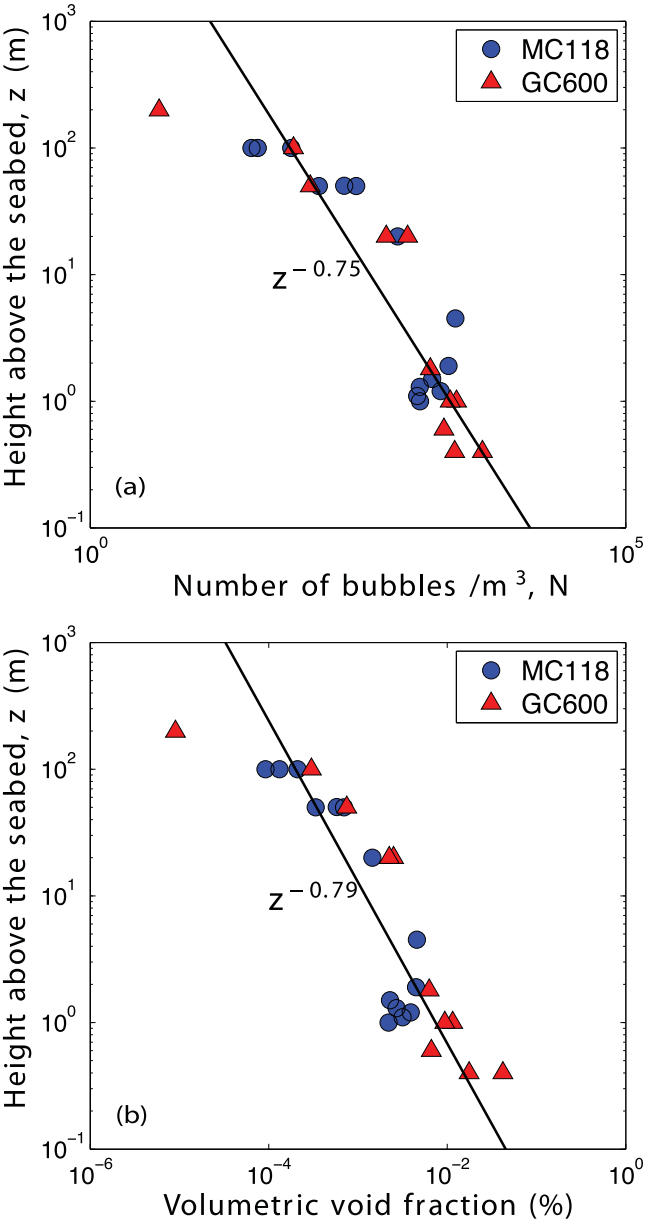

Figure 18. Profile of (a) population density of bubbles and (b) volumetric void fraction above the seafloor at the two seep sites.

and due to the larger bubbles observed at GC 600 compared to MC 118, which also contain more mass and dissolve slower (because they have a lower surface area to volume ratio). The correspondence of the observed rise heights with the boundary of the HSZ is likely coincidental. Seep bubbles dissolve under the HSZ and shrink during the entire height-of-rise. According to measured shrinkage rate and dissolution (see section 3.6.3), small bubbles (<5 mm) may dissolve completely into the water column before reaching the boundary of the HSZ. Only large bubbles likely survive to the top of the flare observed close to or above the HSZ. Numerical models can be used to predict the height-of-rise [*McGinnis et al.*, 2006; *Römer et al.*, 2012], and this is part of our ongoing development of the TAMOC model.

3.6.3. Estimation of Dissolution Rates

As the bubbles rise through the water column, their size is also expected to change as a result of expansion by pressure (increasing their size), dissolution (decreasing their size since the hydrocarbon gases leave the bubble faster than atmospheric gases diffuse in), and fractionation (sorting of size caused by the currents). The effect of pressure is relatively weak (pressure decreases by about 10% over 100 m from 1000 m depth) and can be predicted by the real gas equation of state. Dissolution is the dominant effect among these factors, which results in the shrinking bubble size while rising. Sorting occurs quickly near the plume source (see, for instance, Figure 17 for the plume signatures at 10 m height), and because of this, we expect that sampling the center of the largest M3 sonar return will give repeated samples of the same population of bubbles at each depth so that our measurements can be applied to estimate dissolution rates.

Figure 20 shows the evolution of the bubble size distribution statistics with height for the two main vent sites. The data in Figure 20a include population and volume distribution measures for D_{50}, the median of the distribution, which also corresponds to the peak diameter, and D_{95}, the diameter which bounds 95% of the measured data. Measurements at Sleeping Dragon only extended to 100 m altitude since we had inadequate time during those dives (generally due to poor weather conditions) to measure reliable statistics at 200 m altitude. Measurements at GC 600 could be quantified to 200 m altitude.

The data in Figure 20b can be used to infer a rough approximation of the dissolution rates of bubbles for the central column of the flare plumes. Here we examine the changes throughout the height-of-rise at GC 600 since these give the largest travel distance and, hence, the lowest error of the estimate. Moreover, we

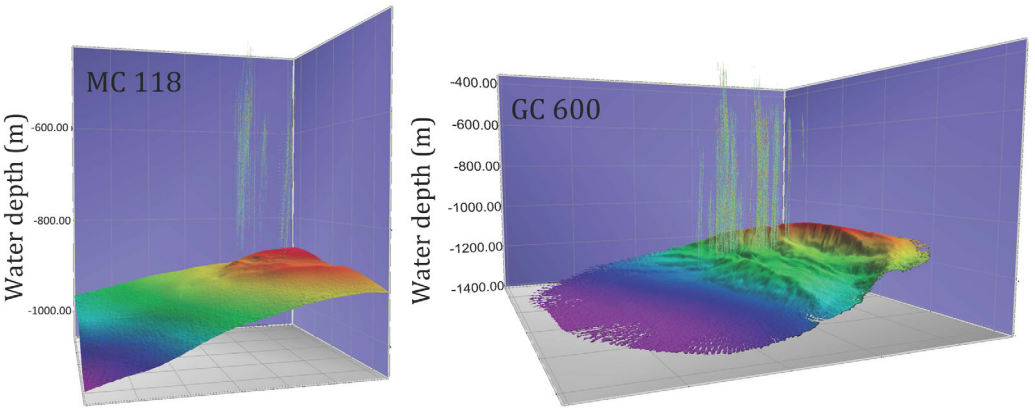

Figure 19. Seep flares imaged by multibeam surveying at two sites. Bottom color shows the topography of the seafloor; water column colors show the intensity of the hydroacoustic anomaly.

apply these calculations to the volume distribution statistics because they are less affected by loss of small bubbles by the currents. At each measurement altitude, we calculate the effective bubble diameters, which are those for each bubble if it were subjected to the pressure at the 200 m height. This calculation is possible by determining the dilation of a constant volume sphere as it is compressed isothermally from 200 m height to the sea floor. The remaining shrinkage trend of the data is the result of dissolution. To estimate this shrinkage rate, we fit a linear regression to all of the measurements. We acknowledge that the bubble shrinkage rate is not a constant during the ascent; however, this is a common estimate reported in the literature.

Based on the linear regressions, the average bubble radius shrinkage rate is 2.82 μm/m at GC 600 over the first 200 m of rise. The goodness of fit of this regression has an $r^2 = 0.94$. Accounting for the average rise velocity, this value for shrinkage rate is equivalent to $dr/dt = -0.42$ μm/s, which agrees well with the result of recent laboratory studies [*Warzinski et al*., 2014, 2014b].

The effective shrinkage rate can be related to mass transfer. The equation for dissolution can be written as

$$\frac{dr}{dz} = -\frac{\beta \Delta C}{\rho_p u_s} \tag{4}$$

where β is the mass transfer coefficient, ΔC is the difference between the solubility and ambient concentration of the dissolving species, ρ_p is the bubble density, and u_s is the slip velocity of the bubbles [*Socolofsky et al*., 2015]. If we assume that methane is the dominant species to dissolve over the 200 m rise, then ΔC can be taken as the solubility of methane from this mixture (1.96 kg/m^3 for 90.2 mol % methane at 1000 m depth), assuming a background concentration of effectively zero. The average density of the bubble over this range is 115 kg/m^3. From section 3.4, the rise velocity for bubbles in the diameter range of 4–8 mm is 0.15 m/s. Taking these values with the shrinkage rate for bubble radius, we obtain $\beta = 2.5 \times 10^{-5}$ m/s. This value compares well with the value computed for methane in the measured natural gas mixture by TAMOC for a 4.5 mm diameter bubble (i.e., the mean bubble size over this rise height) of 3.8×10^{-5} m/s. Using the diffusivity D of methane in seawater of 8×10^{-10} m^2/s with this mean bubble size gives a Sherwood number of $Sh = d\beta/D = 140$. This value corresponds well with measured Sherwood numbers for dirty bubbles, which are in the range of 100–200 for this size of bubble [*Clift et al*., 1978].

If we apply the same analysis to the larger bubbles given by D_{95}, we obtain a mass transfer coefficient of $\beta = 7.2 \times 10^{-5}$ m/s. This value is higher than the corresponding value computed for a 6.2 mm bubble in TAMOC of 3.2×10^{-5} m/s. The Sherwood number for the measured shrinkage rate gives $Sh = 556$, which is closer to the Sherwood numbers reported for clean bubbles in this bubble size range, which span 600–1200 [*Clift et al*., 1978]. In addition, this shrinkage rate corresponds to about 1.2 μm/s, which is higher than those observed in the laboratory settings [*Warzinski et al*., 2014, 2014b]. One possible explanation is that these larger bubbles indeed dissolve at rates similar to the clean bubble solubility. We believe this is unlikely given the fact that the interface is observed to be immobile and that bubbles in this size range were

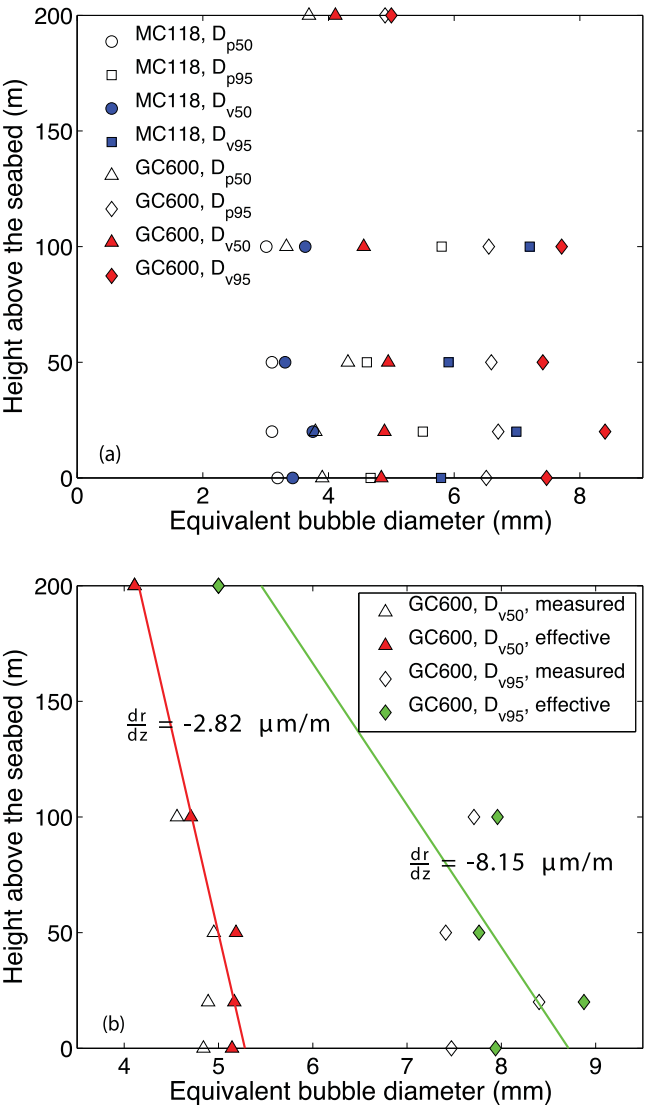

Figure 20. Profile of bubble size above the seabed. (a) Equivalent bubble diameters are reported in D_{50} and D_{95} calculated from the cumulative distribution function in terms of population (subscript *p*) and volume (subscript *v*). (b) Effective bubble diameters due to expansion by pressure between the measurement altitudes and 200 m. The solids lines are the linear regression lines to the data, indicating bubble shrinkage.

observed in the oceans to dissolve at the dirty bubble rate after a short transition time by *Rehder et al*. [2009]. Another, more likely explanation is that the extremes of the distribution were undersampled due to the spreading and the low number of bubbles per sample volume at 200 m height. From Figure 18, the bubble concentration per volume decreased by about 3.5 orders of magnitude from the source to a height of 200 m. Because we could not sample for an equivalently longer time, our estimate of D_{95} is likely biased to smaller diameters at 200 m than the full distribution would have (i.e., we did not measure enough of the large diameters to resolve the tail of the distribution). Smaller diameters imply more dissolution, which is giving a false estimate of the mass transfer. Hence, the mass transfer rates for the mean are estimated well for these data, but estimates for the tails of the distribution are biased by sampling error as we move up in the plume. Likewise, these shrinkage rates are specific to the given diameter and gas composition and are not universal for all bubbles at all seeps.

4. Conclusions

In this paper, we present an analysis of the high-speed, stereoscopic TAMU-CAM image data collected during the GISR G07 cruise on the *E/V Nautilus* to two natural gas seep sites in the northern Gulf of Mexico (MC 118 and GC 600). From qualitative analysis of the image data, we can infer that bubbles rise largely independently, with little bubble-bubble or bubble-water interaction and negligible plume effect above 1.5 m above the sources. The high-speed imagery also demonstrates that the bubble-water interface is rigid above 1.3–1.5 m height at all sites, indicating the presence of a clathrate hydrate shell. Quantitative analysis of the images yielded measurements of the bubble size distribution, the rise velocity, the trajectories of individual bubbles, the total seep gas flux, the plume growth in the water column, the volumetric void fraction, and the dissolution over the first 200 m of rise above the sea floor. Multibeam imaging further documents that the height-of-rise of each flare was to a depth of about 400 m at MC 118 and 350 m at GC 600, near the hydrate stability zone boundary for the released natural gas mixtures.

The bubble size distributions were stable at the two primary vents (Sleeping Dragon in MC 118 and Confetti plume in GC 600), and the measurements from each dive fitted well a lognormal distribution for the population and volume PDFs of bubble size. The secondary vents in GC 600 (Old Reliable and Louie the King) had more unsteady emission on the time scale of tens of seconds, with bubble sizes alternating between smaller and larger bubbles. But the gas flux converges on a time scale of tens of minutes. Across all the

measurements, the peak bubble size (most probable size in the volume distribution) ranged from 3 to 4.5 mm. The bubble layer distributions in volume showed power law dependencies, growing with rates of $S_L' = 4.4–7.7$ for sizes smaller than the peak diameter, and decaying with rates of $S_L = -4.6$ to -8.6 for sizes larger than the peak diameter. Comparing to previous reported values [*Leifer and MacDonald*, 2003], these rates are faster, indicating that our observed size distributions are narrower than those previously reported. The smallest observed bubbles were 1.1 mm at MC 118 and 0.8 mm at GC 600.

From an analysis of our bubble rise velocity data, two different characteristic rise velocities were observed: a faster rise velocity corresponding to empirical equations for terminal rise velocity of dirty ellipsoidal bubbles in *Clift et al*. [1978] and a slower velocity about 40% lower for the same size and shape range. By tracking individual bubbles in the stereoscopic TAMU-CAM system, we correlated the faster-rising bubbles with those following a helical path trajectory, and the slower-rising bubbles with those in a zig-zag trajectory pattern. Most of the bubbles measured for each of the dives tracked the slower rise velocity. However, the slow and fast rise velocity did not correspond to hydrate formation, and both types of bubble trajectory were observed at both sites.

Moving up the water column, currents stretched the flares, sorting bubbles by their rise velocity. Dissolution rates were evaluated from the bubble size distributions computed at the seafloor and at 200 m altitude for GC 600. The shrinkage rate of bubbles in the center of the distribution agreed very well with mass transfer rates for dirty bubbles. For the larger bubble sizes in the tail of the volume distribution, the mass transfer rates appeared greater. This was attributed to undersampling of the distribution for the dilute plume at 200 m; hence, the mass transfer should only be estimated from the median of the volume distribution for this data set.

Taken together, these observations give a comprehensive view of bubble dynamics in these seep flares. Gas bubbles originate at their sources as free gas, with sizes between 1 and 8 mm diameter, most common diameters of 3–4 mm, and following a lognormal distribution. At these depths (about 1000 m), hydrate skins form on the bubble-water interface within about 10 s of rise time, and the larger bubbles continue to rise to a height close to the boundary of the hydrate stability zone. The majority of bubbles follow a zig-zag path, that leads to a rise velocity about 40% lower than the terminal rise velocity predicted by the empirical equations for ellipsoidal bubbles in *Clift et al*. [1978]; however, some bubbles rise in helical paths that match closely the *Clift et al*. [1978] predictions, and there is no explicit correlation between rise velocity and hydrate formation. During their rise through the water column, ambient currents strip entrained fluid from the plume so that plume growth is dominated by turbulent processes in the across-stream direction and slip-velocity sorting in the along-stream direction. Dissolution rates of the median bubble sizes match closely to those for dirty bubbles, with no apparent reduction in mass transfer resulting from the hydrate shells. Hence, these seep bubbles behaved similarly to individual dirty natural gas bubbles rising through the ambient currents.

Acknowledgments

This research was made possible by a grant from the Gulf of Mexico Research Initiative to the Gulf Integrated Spill Research (GISR) Consortium. Data are publicly available through the Gulf of Mexico Research Initiative Information & Data Cooperative (GRIIDC) at https://data.gulfresearchinitiative.org (doi:10.7266/N7VM4969, doi:10.7266/N7QV3JGK, and doi:10.7266/N7N014GM). The authors thank the scientists, crew, and the data group of the *E/V Nautilus*, especially the operators of *ROV Hercules* and *Argus* for their delicate work during the GISR G07 cruise.

References

Anderson, K., et al. (2012), Hydrates in the ocean beneath, around, and above production equipment, *Energy Fuels*, *26*(7), 4167–4176, doi:10.1021/Ef300261z.

Breier, J. A. (2015), Gisr: G07 field survey: Methane concentrations in gas plumes from Mississippi and Green Canyon seeps in July 2014. Distributed by Gulf of Mexico Research Initiative Information and Data Cooperative (GRIIDC), Harte Res. Inst., Texas A&M Univ., Corpus Christi, Corpus Christi, doi:10.7266/N7N014GM.

Breier, J. A., et al. (2014), A large volume particulate and water multi-sampler with *in situ* preservation for microbial and biogeochemical studies, *Deep Sea Res., Part I*, *94*, 195–206, doi:10.1016/j.dsr.2014.08.008.

Chen, F. H., and P. D. Yapa (2001), Estimating hydrate formation and decomposition of gases released in a deepwater ocean plume, *J. Mar. Syst.*, *30*(1–2), 21–32.

Chen, F. H., and P. D. Yapa (2004), Modeling gas separation from a bent deepwater oil and gas jet/plume, *J. Mar. Syst.*, *45*(3–4), 189–203.

Clift, R., J. R. Grace, and M. E. Weber (1978), *Bubbles, Drops, and Particles*, xiii, 380 pp., Academic, N. Y.

Du, M. R., and J. D. Kessler (2012), Assessment of the spatial and temporal variability of bulk hydrocarbon respiration following the Deepwater Horizon oil spill, *Environ. Sci. Technol.*, *46*(19), 10,499–10,507, doi:10.1021/es301363k.

Fischer, H. B., E. G. List, R. C. Y. Koh, J. Imberger, and N. H. Brooks (1979), *Mixing in Inland and Coastal Waters*, Academic, N. Y.

Granin, N. G., M. M. Makarov, K. M. Kucher, and R. Y. Gnatovsky (2010), Gas seeps in Lake Baikal-detection, distribution, and implications for water column mixing, *Geo Mar. Lett.*, *30*(3–4), 399–409, doi:10.1007/s00367-010-0201-3.

Greinert, J., Y. Artemov, V. Egorov, M. De Batist, and D. McGinnis (2006), 1300 m-high rising bubbles from mud volcanoes at 2080 m in the Black Sea: Hydroacoustic characteristics and temporal variability, *Earth Planet. Sci. Lett.*, *244*(1–2), 1–15, doi:10.1016/J.Epsl.2006.02.01.

Johansen, O. (2000), DeepBlow—A Lagrangian plume model for deep water blowouts, *Spill Sci. Technol. Bull.*, *6*(2), 103–111.

Johansen, O. (2003), Development and verification of deep-water blowout models, *Mar. Pollut. Bull.*, *47*(9–12), 360–368, doi:10.1016/S0025-326X(03)00202-9.

Kessler, J. D., et al. (2011), A persistent oxygen anomaly reveals the fate of spilled methane in the deep Gulf of Mexico, *Science*, *331*(6015), 312–315, doi:10.1126/science.1199697.

Laqua, K., K. Malone, M. Hoffmann, D. Krause, and M. Schlüter (2016), Methane bubble rise velocities under deep-sea conditions—influence of initial shape deformation, *Colloids Surf. A*, doi:10.1016/j.colsurfa.2016.01.041.

Leifer, I. (2010), Characteristics and scaling of bubble plumes from marine hydrocarbon seepage in the Coal Oil Point seep field, *J. Geophys. Res.*, *115*, C11014, doi:10.1029/2009JC005844.

Leifer, I., and I. MacDonald (2003), Dynamics of the gas flux from shallow gas hydrate deposits: Interaction between oily hydrate bubbles and the oceanic environment, *Earth Planet. Sci. Lett.*, *210*(3–4), 411–424, doi:10.1016/S0012-821X(03)00173-0.

Levine, J. S., I. Haljasmaa, R. Lynn, F. Shaffer, and R. P. Warzinski (2015), Detection of hydrates on gas bubbles during a subsea oil/gas leak, *Rep. NETL-TRS-6-2015*, Natl. Energy Technol. Lab.

MacDonald, I. R., I. Leifer, R. Sassen, P. Stine, R. Mitchell, and N. Guinasso (2002), Transfer of hydrocarbons from natural seeps to the water column and atmosphere, *Geofluids*, *2*(2), 95–107, doi:10.1046/j.1468-8123.2002.00023.x.

Maini, B. B., and P. R. Bishnoi (1981), Experimental investigation of hydrate formation behavior of a natural-gas bubble in a simulated deep-sea environment, *Chem. Eng. Sci.*, *36*(1), 183–189, doi:10.1016/0009-2509(81)80062-0.

McGinnis, D. F., J. Greinert, Y. Artemov, S. E. Beaubien, and A. Wuest (2006), Fate of rising methane bubbles in stratified waters: How much methane reaches the atmosphere?, *J. Geophys. Res.*, *111*, C09007, doi:10.1029/2005JC003183.

Milgram, J. H. (1983), Mean flow in round bubble plumes, *J. Fluid Mech.*, *133*, 345–376.

Rehder, G., R. W. Collier, K. Heeschen, P. M. Kosro, J. Barth, and E. Suess (2002), Enhanced marine CH_4 emissions to the atmosphere off Oregon caused by coastal upwelling, *Global Biogeochem. Cycles*, *16*(3), doi:10.1029/2000GB001391.

Rehder, G., I. Leifer, P. G. Brewer, G. Friederich, and E. T. Peltzer (2009), Controls on methane bubble dissolution inside and outside the hydrate stability field from open ocean field experiments and numerical modeling, *Mar. Chem.*, *114*(1–2), 19–30, doi:10.1016/j.marchem.2009.03.004.

Römer, M., H. Sahling, T. Pape, G. Bohrmann, and V. Spiess (2012), Quantification of gas bubble emissions from submarine hydrocarbon seeps at the Makran continental margin (offshore Pakistan), *J. Geophys. Res.*, *117*, C10015, doi:10.1029/2011JC007424.

Ryerson, T. B., et al. (2011a), Atmospheric emissions from the Deepwater Horizon spill constrain air-water partitioning, hydrocarbon fate, and leak rate, *Geophys. Res. Lett.*, *38*, L07803, doi:10.1029/2011GL046726.

Ryerson, T. B., et al. (2011b), Chemical data quantify Deepwater Horizon hydrocarbon flow rate and environmental distribution, *Proc. Natl. Acad. Sci.*, *109*, 20,246–20,253, doi:10.1073/pnas.1110564109.

Sachs, W., and V. Meyn (1995), Pressure and temperature dependence of the surface tension in the system natural gas/water principles of investigation and the first precise experimental data for pure methane water at 25°C up to 46.8 MPa, *Colloids Surf. A*, *94*(2–3), 291–301, doi:10.1016/0927-7757(94)03008-1.

Sahling, H., et al. (2009), Vodyanitskii mud volcano, Sorokin trough, Black Sea: Geological characterization and quantification of gas bubble streams, *Mar. Pet. Geol.*, *26*(9), 1799–1811, doi:10.1016/j.marpetgeo.2009.01.010.

Sauter, E. J., S. I. Muyakshin, J. L. Charlou, M. Schluter, A. Boetius, K. Jerosch, E. Damm, J. P. Foucher, and M. Klages (2006), Methane discharge from a deep-sea submarine mud volcano into the upper water column by gas hydrate-coated methane bubbles, *Earth Planet. Sci. Lett.*, *243*(3–4), 354–365, doi:10.1016/j.epsl.2006.01.041.

Seewald, J. S., K. W. Doherty, T. R. Hammar, and S. P. Liberatore (2002), A new gas-tight isobaric sampler for hydrothermal fluids, *Deep Sea Res., Part I*, *49*(1), 189–196, doi:10.1016/S0967-0637(01)00046-2.

Sloan, E. D., and C. A. Koh (2008), *Clathrate Hydrates of Natural Gases*, 3rd ed., CRC Press, N. Y.

Socolofsky, S. A. (2015a), High-definition videos of natural gas seeps observed at the seafloor and in the water column on GISR Cruise G07 at GC 600 and MC 118 in July 2014. Distributed by Gulf of Mexico Research Initiative Information and Data Cooperative (GRIIDC), Harte Res. Inst., Tex. A&M Univ., Corpus Christi, Corpus Christi, doi:10.7266/N7VM4969.

Socolofsky, S. A. (2015b), Stereoscopic high-speed high-resolution camera images of natural gas seeps observed at the seafloor and in the water column on GISR Cruise G07 at GC 600 and MC 118 in July 2014. Distributed by Gulf of Mexico Research Initiative Information and Data Cooperative (GRIIDC), Harte Res. Inst., Tex. A&M Univ., Corpus Christi, Corpus Christi, doi:10.7266/N7QV3JGK.

Socolofsky, S. A., and E. E. Adams (2002), Multi-phase plumes in uniform and stratified crossflow, *J. Hydraul. Res.*, *40*(6), 661–672.

Socolofsky, S. A., E. E. Adams, and C. R. Sherwood (2011), Formation dynamics of subsurface hydrocarbon intrusions following the Deepwater Horizon blowout, *Geophys. Res. Lett.*, *38*, L09602, doi:10.1029/2011GL047174.

Socolofsky, S. A., A. L. Dissanayake, I. Jun, J. Gros, J. S. Arey, and C. M. Reddy (2015), *Texas A&M Oilspill Calculator (TAMOC): Modeling Suite for Subsea Spills*., 38th AMOP Technical Seminar on Environmental Contamination and Response, Vancouver, B. C., Canada, June 2–4.

Spier, C., W. T. Stringfellow, T. C. Hazen, and M. Conrad (2013), Distribution of hydrocarbons released during the 2010 MC252 oil spill in deep offshore waters, *Environ. Pollut.*, *173*, 224–230, doi:10.1016/j.envpol.2012.10.019.

Thomanek, K., O. Zielinski, H. Sahling, and G. Bohrmann (2010), Automated gas bubble imaging at sea floor—A new method of *in situ* gas flux quantification, *Ocean Sci.*, *6*(2), 549–562, doi:10.5194/os-6-549-2010.

Tomiyama, A., G. P. Celata, S. Hosokawa, and S. Yoshida (2002), Terminal velocity of single bubbles in surface tension force dominant regime, *Int. J. Multiphase Flow*, *28*, 1497–1519.

Valentine, D. L., et al. (2010), Propane respiration jump-starts microbial response to a deep oil spill, *Science*, *330*(6001), 208–211, doi:10.1126/science.1196830.

Wang, B., and S. A. Socolofsky (2015a), A deep-sea, high-speed, stereoscopic imaging system for *in situ* measurement of natural seep bubble and droplet characteristics, *Deep Sea Res., Part A*, *104*, 134–148.

Wang, B., and S. A. Socolofsky (2015b), On the bubble rise velocity of a continually released bubble chain in still water and with crossflow, *Phys. Fluids*, *27*(10), 103301, doi:10.1063/1.4932176.

Warzinski, R. P., R. Lynn, I. Haljasmaa, I. Leifer, F. Shaffer, B. J. Anderson, and J. S. Levine (2014), Dynamic morphology of gas hydrate on a methane bubble in water: Observations and new insights for hydrate film models, *Geophys. Res. Lett.*, *41*, 6841–6847, doi:10.1002/2014GL061665.

Warzinski, R. P., F. Shaffer, R. Lynn, I. Haljasmass, M. Schellhaas, B. Anderson, S. Velaga, I. Leifer, and J. Levine (2014b), Department of Energy, National Energy Technology Laboratory, The Role of Gas Hydrates during the Release and Transport of Well Fluids in the Deep Ocean, Bureau of Safety and Environmental Enforcement, Herndon, Va. [Available at http://www.bsee.gov/Technology-and-Research/Oil-Spill-Response-Research/Projects/Project-698/.]

Weber, T. C., L. Mayer, K. Jerram, J. Beaudoin, Y. Rzhanov, and D. Lovalvo (2014), Acoustic estimates of methane gas flux from the seabed in a 6000 km^2 region in the northern Gulf of Mexico, *Geochem. Geophys. Geosyst.*, *15*, 1911–1925, doi:10.1002/2014GC005271.

Wu, M. M., and M. Gharib (2002), Experimental studies on the shape and path of small air bubbles rising in clean water, *Phys. Fluids*, *14*(7), L49–L52, doi:10.1063/1.1485767.

Yapa, P. D., and F. H. Chen (2004), Behavior of oil and gas from deepwater blowouts, *J. Hydraul. Eng.*, *130*(6), 540–553.

Yapa, P. D., and L. Zheng (1997), Simulation of oil spills from underwater accidents. 1. Model development, *J. Hydraul. Res.*, *35*(5), 673–687.

Yapa, P. D., L. Zheng, and K. Nakata (1999), Modeling underwater oil/gas jets and plumes, *J. Hydraul. Eng.*, *125*(5), 481–491.

Yvon-Lewis, S., L. Hu, and J. D. Kessler (2011), Methane flux to the atmosphere from the Deepwater Horizon oil disaster, *Geophys. Res. Lett.*, *38*, L01602, doi:10.1029/2010GL045928.

Zheng, L., and P. D. Yapa (2000), Buoyant velocity of spherical and nonspherical bubbles/droplets, *J. Hydraul. Eng.*, *126*(11), 852–854.

Zheng, L., and P. D. Yapa (2002), Modeling gas dissolution in deepwater oil/gas spills, *J. Mar. Syst.*, *31*(4), 299–309.